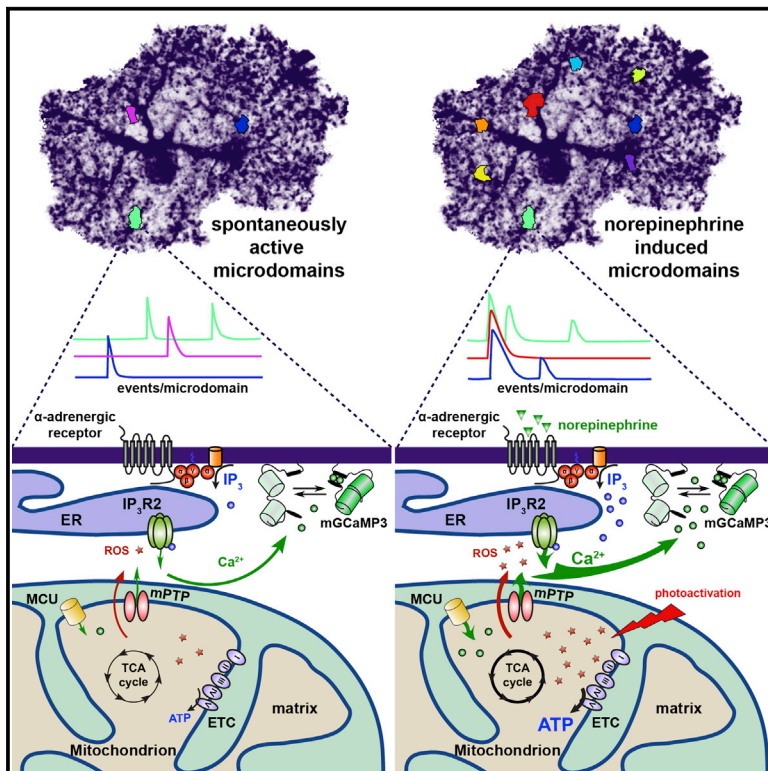


Neuron

Transient Opening of the Mitochondrial Permeability Transition Pore Induces Microdomain Calcium Transients in Astrocyte Processes

Graphical Abstract



Authors

Amit Agarwal, Pei-Hsun Wu,
Ethan G. Hughes, ...,
Abraham J. Langseth, Denis Wirtz,
Dwight E. Bergles

Correspondence

dbergles@jhmi.edu

In Brief

Agarwal et al. show that mitochondria in the fine processes of astrocytes produce spatially localized Ca^{2+} transients through brief openings of the mitochondrial transition pore, linking microdomain Ca^{2+} signaling in these ubiquitous glial cells to metabolic demand and mitochondrial stress.

Highlights

- Membrane-anchored GCaMP3 mice facilitate detection of microdomain Ca^{2+} transients
- Mitochondria are localized to microdomains in astrocyte processes
- Permeability transition pore opening causes microdomain mitochondrial Ca^{2+} events
- Mitochondria-induced events are enhanced by neuronal activity and mutant SOD1



Transient Opening of the Mitochondrial Permeability Transition Pore Induces Microdomain Calcium Transients in Astrocyte Processes

Amit Agarwal,¹ Pei-Hsun Wu,² Ethan G. Hughes,^{1,5} Masahiro Fukaya,⁴ Max A. Tischfield,^{3,6} Abraham J. Langseth,¹ Denis Wirtz,² and Dwight E. Bergles^{1,7,*}

¹The Solomon H. Snyder Department of Neuroscience

²Department of Chemical and Biomolecular Engineering

³Department of Molecular Biology and Genetics

Johns Hopkins University School of Medicine, Baltimore, MD 21205, USA

⁴Department of Anatomy, Kitasato University School of Medicine, Sagamihara 252-0374, Japan

⁵Present address: Department of Cell and Developmental Biology, University of Colorado School of Medicine, Aurora, CO 80045, USA

⁶Present address: Department of Neurology, Children's Hospital Boston and Harvard Medical School, Boston, MA 02115, USA

⁷Lead Contact

*Correspondence: dbergles@jhmi.edu

<http://dx.doi.org/10.1016/j.neuron.2016.12.034>

SUMMARY

Astrocytes extend highly branched processes that form functionally isolated microdomains, facilitating local homeostasis by redistributing ions, removing neurotransmitters, and releasing factors to influence blood flow and neuronal activity. Microdomains exhibit spontaneous increases in calcium (Ca^{2+}), but the mechanisms and functional significance of this localized signaling are unknown. By developing conditional, membrane-anchored GCaMP3 mice, we found that microdomain activity that occurs in the absence of inositol triphosphate (IP3)-dependent release from endoplasmic reticulum arises through Ca^{2+} efflux from mitochondria during brief openings of the mitochondrial permeability transition pore. These microdomain Ca^{2+} transients were facilitated by the production of reactive oxygen species during oxidative phosphorylation and were enhanced by expression of a mutant form of superoxide dismutase 1 (SOD1 G93A) that causes astrocyte dysfunction and neurodegeneration in amyotrophic lateral sclerosis (ALS). By localizing mitochondria to microdomains, astrocytes ensure local metabolic support for energetically demanding processes and enable coupling between metabolic demand and Ca^{2+} signaling events.

INTRODUCTION

Astrocytes are ubiquitous glial cells in the central nervous system that are highly conserved in both form and function from flies to mammals (Freeman and Rowitch, 2013). They are distributed in a grid-like manner, with cells spaced equidistant from one another, and extend highly ramified processes into the neuropil,

forming a dense meshwork in which neurons, blood vessels, and other glial cells are embedded (Kosaka and Hama, 1986). Astrocyte processes consist of thin lamellar sheets that are responsible for performing essential homeostatic processes that consume considerable energy, such as restoring ion gradients, removing neurotransmitters, and refining neural networks. These membranous elaborations are often coupled to the rest of the cell by narrow cytoplasmic channels, creating functionally isolated "microdomains" that may restrict diffusion and allow astrocytes to adapt their physiology to local demands (Grosche et al., 1999). Despite the crucial importance of astrocyte microdomains in brain homeostasis, we know little about their functional characteristics or the dynamics of signaling in these restricted volumes, information that is essential to define how astrocytes contribute to brain function and dysfunction.

Because of their wide distribution and complex morphology, astrocytes are ideally situated to provide both global support of neural circuits and exert local control over active synapses (Araque et al., 2014). They express a variety of neurotransmitter receptors, in particular, metabotropic receptors that induce transient increases in intracellular Ca^{2+} . In vivo studies in awake mice indicate that astrocytes throughout the brain experience Ca^{2+} increases when norepinephrine (NE) is released during periods of increased arousal, indicating that they are co-activated with neurons during state transitions (Paukert et al., 2014). In addition to these global changes in activity, astrocytes also exhibit spontaneous increases in Ca^{2+} within microdomains that appear to be cell autonomous (Nett et al., 2002), because they occur in the absence of neuronal input and persist when astrocytes are maintained in isolation (Khakh and McCarthy, 2015). Ca^{2+} changes in astrocytes can enhance glucose mobilization, alter hemodynamics, and influence the activity of surrounding neurons and glia by releasing neuroactive compounds such as ATP, D-serine, and glutamate (Haydon, 2001). In addition, astrocyte Ca^{2+} transients occur more frequently following CNS injury and are enhanced in regions of amyloid deposition in the Alzheimer's model mice (Kuchibhotla et al., 2009), demonstrating that this signaling is highly adaptable and dependent on the activity level

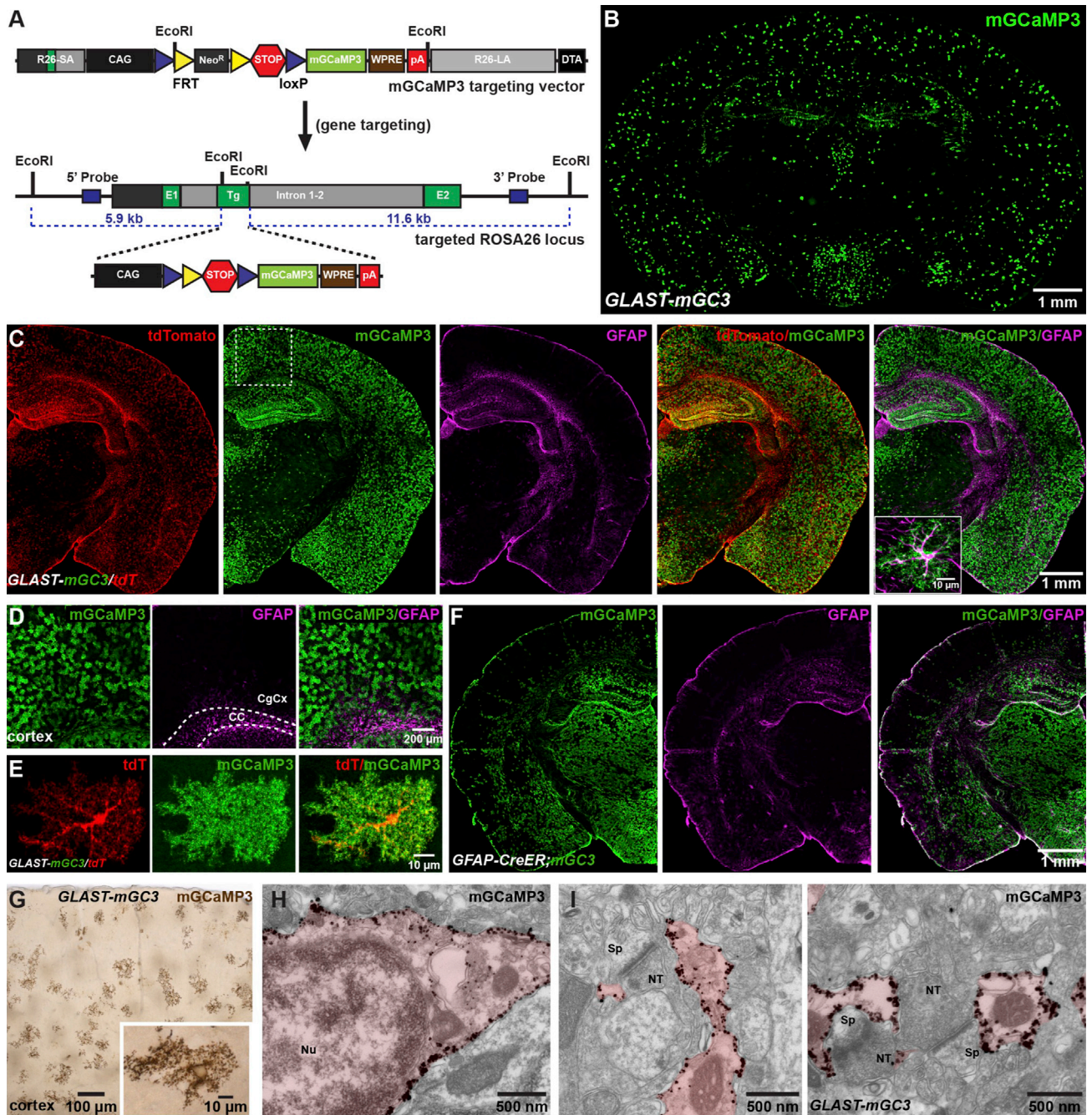


Figure 1. Conditional Expression of mGCaMP3 in Astrocytes

(A) Gene trap strategy used to insert conditional mGCaMP3 transgene into murine *Rosa26* gene. (Top) mGCaMP3 targeting vector that harbors 5' short (R26-SA) and 3' long (R26-LA) homology arms from *Rosa26*, the CMV enhancer chicken β -actin hybrid (CAG) promoter (black box), loxP (blue triangles), neomycin resistance cassette (NeoR, gray box) flanked by two FRT sites (yellow triangles) and 3 \times SV40-polyA sequence (red hexagon), the mGCaMP3 cDNA (light green box), woodchuck post-transcriptional response element (WPRE; brown box), bovine growth hormone poly A sequence (red box), and negative selection cassette with diphtheria toxin fragment A (DTA; black box). (Bottom) *Rosa26* allele with conditional mGCaMP3 cassette after homologous recombination. NeoR cassette was removed by in vivo site-specific recombination.

(B) Coronal section of brain from a *GLAST-CreER;Rosa26-*Isl*-mGCaMP3* (*GLAST-mGCaMP3*) mouse immunostained for mGCaMP3.

(C) Coronal hemi-section of brain from a *GLAST-CreER;Rosa26-*Isl*-mGCaMP3;Rosa26-*Isl*-tdTomato* (*GLAST-mGCaMP3/tdT*) mouse immunostained for tdTomato, mGCaMP3, and GFAP. Inset shows one cortical astrocyte at higher magnification co-expressing mGCaMP3 and GFAP.

(D) High-magnification images from boxed area in (C).

(E) Images showing one cortical astrocyte from a *GLAST-mGCaMP3/tdT* mouse (maximum intensity projected confocal z stack) immunostained for mGCaMP3 and tdT.

(legend continued on next page)

of surrounding neurons. Nevertheless, the mechanisms that control Ca^{2+} signaling in astrocyte microdomains have remained uncertain, and their relationship to receptor-mediated Ca^{2+} transients has not been defined.

To determine the mechanisms responsible for inducing localized Ca^{2+} signaling in astrocytes, we developed conditional transgenic mice in which a membrane-anchored form of the genetically encoded Ca^{2+} sensor mGCaMP3 could be expressed selectively within astrocytes, and developed software based on machine learning for unbiased selection and analysis of active domains. We show that spatially restricted Ca^{2+} transients in astrocyte processes that occur independent of release from ER stores are caused by Ca^{2+} efflux from mitochondria, in response to transient opening of the permeability transition pore (mPTP).

RESULTS

Generation of Conditional, Membrane-Anchored mGCaMP3 Mice

Astrocyte processes extend thin lamellar sheets that contain minimal cytoplasm, presenting challenges for detection of Ca^{2+} changes with cytosolic indicators. To facilitate analysis of microdomain Ca^{2+} signaling in situ, we generated a transgenic mouse line in which a Cre-dependent allele encoding a membrane-anchored variant of the genetically encoded calcium indicator mGCaMP3 (Tian et al., 2009) (mGCaMP3) was knocked into the Rosa26 locus (Figure 1A) (see STAR Methods). To express mGCaMP3 specifically in astrocytes, we bred these *Rosa26-*Isl*-mGCaMP3* mice to *GLAST-CreER* BAC transgenic mice (Paukert et al., 2014) and induced mGCaMP3 expression by injecting tamoxifen intraperitoneally (i.p.). Immunohistochemical analysis of *GLAST-CreER;Rosa26-*Isl*-mGCaMP3* (*GLAST-mGC3*) mice several weeks after tamoxifen injection revealed that mGCaMP3 was expressed by astrocytes throughout the brain (Figures 1B and 1C); by lowering the dose of tamoxifen, sparse mGCaMP3 expression could be achieved, allowing unambiguous analysis of individual cells (Figures 1D and 1E). Although minimal recombination was observed in subcortical regions (Figures 1B and 1C), this pattern reflects low CreER expression by astrocytes, rather than differences in ability to express mGCaMP3, because mGCaMP3 was expressed by astrocytes in these regions when *Rosa26-*Isl*-mGCaMP3* mice were bred to *GFAP-CreER* mice (Figure 1F). Postnatal induction of mGCaMP3 expression in these lines did not appear to induce reactive changes in astrocytes, because glial fibrillary acidic protein (GFAP) expression was not increased in the cortex (Figures 1C, 1D, and 1F).

To determine whether mGCaMP3 is targeted to the plasma membrane and present in the fine processes of astrocytes, we crossed *GLAST-mGC3* mice to *Rosa26-*Isl*-tdTomato* (tdT)

(Ai14) mice, allowing visualization of the astrocyte cytosol (Figure 1C). Immunocytochemical analysis revealed a striking difference in the pattern of tdTomato (tdT) and EGFP expression within astrocytes: TdT was present in the soma and main branches of astrocyte processes, whereas mGCaMP3 outlined a larger volume of the cell and enhanced visualization of fine processes (Figure 1E). Electron microscopic (EM) analysis using silver-enhanced immunogold labeling (Figures 1G–1I) revealed that mGCaMP3 was localized to the plasma membrane (Figure 1H) and present within thin lamellar extensions of astrocytes that ensheath synapses (Figure 1I), indicating that this genetic strategy can be used to localize a Ca^{2+} sensor within the finest processes of astrocytes.

Semi-automatic Analysis of Microdomain Ca^{2+} Transients

Astrocytes exhibit global increases in intracellular Ca^{2+} in response to stimulation of metabotropic receptors, as well as spatially restricted, apparently spontaneous Ca^{2+} transients (Nett et al., 2002), the origin of which has not been determined. To assess whether mGCaMP3 is able to resolve these different signals, time-lapse confocal imaging of individual cortical astrocytes was performed in acute brain slices from adult *GLAST-mGC3* (Figures S1A and S1B) and *GLAST-mGC3/tdT* (Figures S1D–S1G) mice. Astrocytes exhibited spontaneous increases in mGCaMP3 fluorescence that were spatially restricted to discrete domains (Figures S1A–S1C; Movie S1), and exposure of slices to agonists for metabotropic glutamate (DHPG [(S)-3,5-Dihydroxyphenylglycine]), 20 μM) or adrenergic receptors (norepinephrine [NE], 10 μM), applied in tetrodotoxin (TTX, 1 μM) to minimize neuronal activation, enhanced Ca^{2+} transients in astrocytes. This activity was qualitatively similar to that observed with Ca^{2+} indicator dyes or through viral delivery of GCaMPs (Di Castro et al., 2011; Shigetomi et al., 2013).

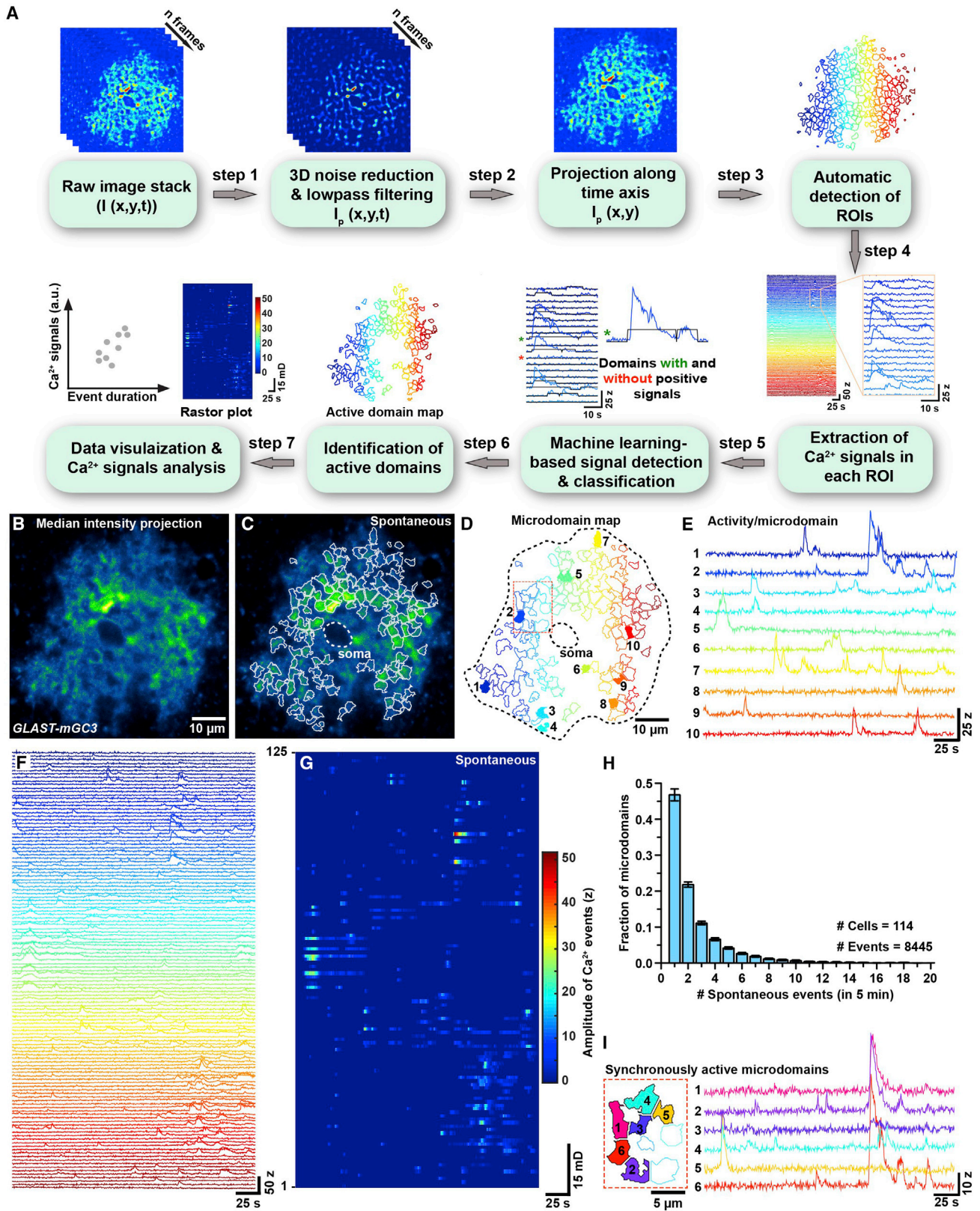
When imaging individual astrocytes with mGCaMP3, Ca^{2+} transients were observed in up to 100 distinct microdomains within the imaging volume, creating new challenges for unbiased analysis of cellular activity based on user-selected regions of interest. To define active regions and extract information about Ca^{2+} dynamics from each location, we developed custom software to perform semi-automated analysis of fluorescence changes (Figure 2A) (see STAR Methods and Data S1). A key feature of this program involves identification of active regions using a machine-learning-based algorithm. We named this software CaSCaDe (Ca^{2+} Signal Classification and Decoding), because each analysis step is dependent on the outcome of the previous step. The CaSCaDe analysis generates a spatial map of regions that exhibit dynamic changes in fluorescence (Figures 2B–2D; Movie S2) and provides information about the number, frequency, amplitude (Z score, see STAR Methods) and time course of events (Figures 2E–2G; Figures S1D–S1P).

(F) Coronal hemi-section of brain from a *GFAP-CreER;Rosa26-*Isl*-mGCaMP3* (*GFAP-CreER;mGC3*) mouse immunostained for mGCaMP3 and GFAP.

(G) Coronal section of brain from a *GLAST-mGC3* mouse showing silver-intensified immunogold labeling of mGCaMP3. Inset shows one astrocyte at higher magnification.

(H and I) High-magnification images of silver-intensified immunogold labeling of mGCaMP3 in an astrocyte soma (H) and peri-synaptic processes (I) from *GLAST-mGC3* mice.

CC, corpus callosum; CgCx, cingulate cortex; NT, nerve terminal; Nu, nucleus; Sp, spine.



(legend on next page)

Analysis of 74 cortical astrocytes revealed that microdomain Ca^{2+} transients occurred frequently throughout the cell (0.67 ± 0.38 Hz), encompassing many distinct sites during a 5 min imaging period (average: 75 ± 30 microdomains). However, activity at each site was infrequent (0.5 ± 0.1 events/min/microdomain), with 69% of microdomains exhibiting only one to two events (Figure 2H), and often uncorrelated with activity at other sites (mean correlation coefficient [ρ], 0.02 ± 0.032), even when active regions were separated by $<10 \mu\text{m}$ (Figure 2I), consistent with the hypothesis that microdomains are functionally isolated (Grosche et al., 1999). Domains that exhibited independent activity could also exhibit highly correlated transients (Figure 2I), suggesting that there are multiple modes of elevating Ca^{2+} within astrocyte processes. Microdomain transients exhibited diverse waveforms, even at individual sites (Figures 2E–2G), and slow kinetics (average duration: 8.5 ± 1.7 s). Although it has been reported that some Ca^{2+} transients in astrocytes are shorter in duration (650–750 ms) (Di Castro et al., 2011), we did not observe such rapid events, even when the sampling rate was increased to 15 Hz (Figures S2A–2H).

Neuromodulators Promote Synchronous Ca^{2+} Elevation in Microdomains

Neurotransmitters, such as NE, that induce Ca^{2+} release from intracellular stores had a profound effect on Ca^{2+} levels in microdomains (Figures 3A and 3B; Movie S2). NE promoted a near-synchronous rise in Ca^{2+} in microdomains (mean correlation coefficient [ρ], 0.49 ± 0.16) (Figures 3C–3F; Movie S2), increased the number of active microdomains per cell by 46%, and enhanced the duration of events at each site by 65% (Figure 3G), but did not increase the frequency of transients within each domain (Figure 3H; Figure S2I). Regions experiencing Ca^{2+} elevations also changed their shape in response to adrenergic receptor stimulation (Figure 3B); nevertheless, for domains that were active during the control period, the site of maximal intensity (centroid) was the same in NE, suggesting that microdomain activity can be influenced by both cell surface receptor activation and cell-intrinsic processes. Unexpectedly, not all spontaneously active microdomains were activated by NE ($71\% \pm 15\%$ overlap; Figure 3I), and stimulation of metabotropic glutamate receptors (DHPG, $10 \mu\text{M}$) or purinergic receptors (ATP, $100 \mu\text{M}$) produced activity maps that were distinct from NE (Figures 3J–3M). Indeed, only 50% of microdomains that were

activated by various agonists overlapped. This could not be explained by trial-to-trial variability, because repetitive application of the same agonist (ATP) resulted in 71% overlap in active domains, despite the small rundown in ATP response to the second stimulus (Figures 3N and 3O). Moreover, only NE was able to induce strong temporal correlation among domains (Figure 3P), suggesting that microdomains are physiologically distinct, contain different combinations of receptors, and can experience different modes of Ca^{2+} increases.

Microdomain Ca^{2+} Transients Can Arise through Cell-Intrinsic Mechanisms

Microdomain Ca^{2+} transients persisted in TTX, but this does not exclude the possibility that they are induced by spontaneous fusion of synaptic vesicles. To address this possibility, we incubated slices in bafilomycin A1 (BafA1; $2 \mu\text{M}$), which depletes vesicles of neurotransmitter, and veratridine ($10 \mu\text{M}$), which promotes opening of voltage-gated Na^+ channels to enhance fusion of already-filled vesicles (Cavelier and Attwell, 2007). Although this manipulation dramatically reduced the frequency and amplitude of spontaneous excitatory postsynaptic currents (sEPSCs) in cortical pyramidal neurons (Figures 4A–4C), microdomain activity in astrocytes persisted (Figures 4D–4I), with the number of active regions (Figure 4H), the frequency of events per microdomain (Figure 4I), and the average amplitude of Ca^{2+} transients (control: 8.3 ± 0.3 , $n = 33$; BafA1: 8.2 ± 0.2 , $n = 36$; $p = 0.71$) unaltered. These findings support the hypothesis that spontaneous microdomain Ca^{2+} transients are intrinsically generated (Nett et al., 2002).

To determine whether spontaneous events detected by mGCaMP3 arise from inositol triphosphate (IP3)-dependent Ca^{2+} release, we monitored spontaneous and evoked microdomain Ca^{2+} transients in mice that lack IP3R2 (Li et al., 2005), which is required for IP3-dependent Ca^{2+} release in astrocytes (Petraovic et al., 2008). The number of active domains was 65% lower in *GLAST-mGCaMP3;IP3R2^{-/-}* mice relative to controls (Figures 4J–4N; Movie S3), and the number of events per domain was significantly reduced, with 83% of microdomains exhibiting only one to two events during the imaging period (Figures 4O and 4P). Moreover, the average event amplitude was significantly reduced in *IP3R2^{-/-}* mice by 1.8 SD (Z score) (*IP3R2^{+/+}*: 10.0 ± 0.2 z, $n = 94$; *IP3R2^{-/-}*: 8.2 ± 0.2 z, $n = 104$; $p < 0.0001$) (Figure 4Q). Similar changes in microdomain activity were observed

Figure 2. Quantification of Spontaneous Microdomain Ca^{2+} Transients in Cortical Astrocytes

- (A) Image analysis based on CaSCaDe (Ca^{2+} Signal Classification and Decoding) algorithm.
 (B) Image of one astrocyte from a *GLAST-mGCaMP3* mouse. Median intensity projection (pseudocolored) from 540 frames.
 (C and D) Maps showing 125 spontaneously active microdomains that occurred in 260 s identified using the CaSCaDe algorithm. (C) All microdomains overlaid on median intensity projected image of astrocyte in (B). (D) Color-coded microdomain map used to uniquely identify each active region. Dashed line indicates cell border.
 (E) Intensity versus time traces for 10 microdomains (from 125) (colors correspond to locations shown in D), showing characteristics of spontaneous Ca^{2+} transients in individual microdomains.
 (F) Intensity versus time traces for 125 spontaneously active microdomains.
 (G) Raster plot of microdomain activity, color-coded according to fluorescence change (Z score).
 (H) Histogram illustrating the number of events that occurred per microdomain in 5 min. Data are shown as mean \pm SEM; 8,445 events were analyzed from 114 cells.
 (I) Spatial map and intensity versus time traces for six adjacent microdomains (area highlighted by red box in D) showing that they can exhibit both uncorrelated and correlated spontaneous activity.

See also Figure S1, Movies S1 and S2, and Data S1.

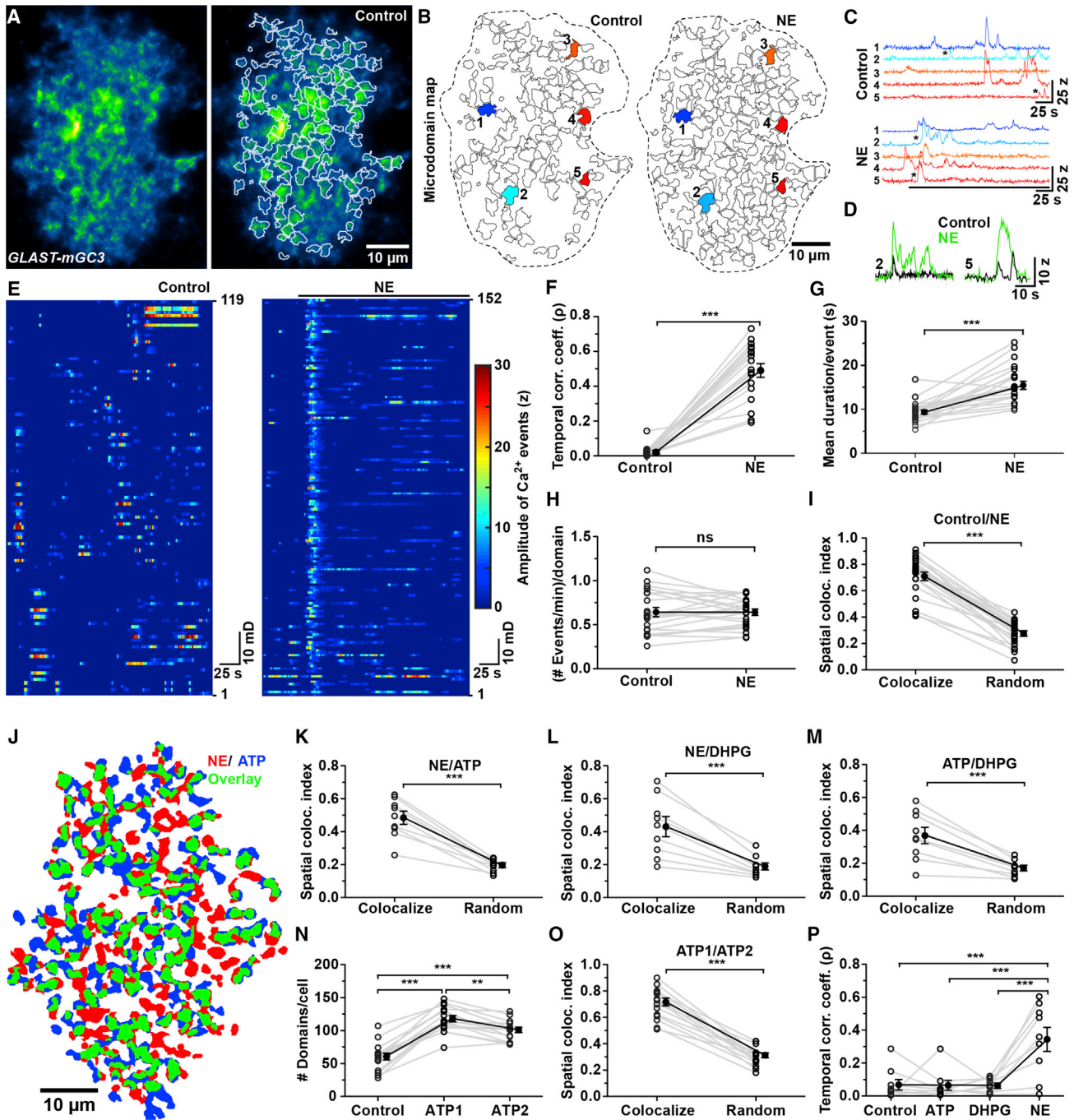


Figure 3. Neurotransmitters Activate Distinct Microdomains in Astrocyte Processes

(A) Median intensity projection image (pseudocolored) of 540 frames from one astrocyte from a *GLAST-mGEC3* mouse (left). Map of spontaneously active microdomains (in TTX, 1 μ M) overlaid on image (right).

(B) Map of microdomains recorded in control (119 domains, left) and after application of norepinephrine (10 μ M NE, 152 domains, right). Dashed lines indicate cell border.

(C) Intensity versus time traces for five microdomains (corresponding to colors in B), showing characteristics of Ca^{2+} transients in control and following application of NE.

(D) Examples of microdomain Ca^{2+} transients from traces 2 and 5 (asterisks in C).

(E) Raster plots displaying timing and intensity of Ca^{2+} transients (119 microdomains in control [left] and 152 microdomains in NE [right]).

(F) Graph of change in temporal correlation of Ca^{2+} transients among microdomains induced by NE (n = 24 cells, *GLAST-mGEC3* mice). Data are shown as mean \pm SEM. ***p < 0.0001; *p = 0.01, paired two-tailed Student's t test.

(legend continued on next page)

following depletion of ER Ca^{2+} stores in $IP3R2^{+/+}$ mice with thapsigargin (Figures S3A–S3E), which prevented NE-induced synchronous microdomain activity (Figure S3F). These results indicate that the reduction of microdomain activity in $IP3R2^{-/-}$ mice does not result from developmental changes, and that there are additional mechanisms that enable cytosolic Ca^{2+} changes in these domains.

If $IP3R2$ is required for enhancing Ca^{2+} transients following stimulation of Gq-coupled receptors, the response to metabotropic receptor agonists should be greatly attenuated. Indeed, no changes were observed in the number of microdomains (Figures 4R–4U), the frequency of events per domain (Figure 4V), or the amplitude of events (Figure 4W) when ATP (100 μM) was applied to cortical slices from $GLAST-mGC3;IP3R2^{-/-}$ mice, supporting the conclusion that $IP3R2$ is the main $IP3R$ subtype in astrocytes, and that other $IP3Rs$ are not upregulated to compensate. Unexpectedly, NE (10 μM) elicited a small increase (24%) in the number of active microdomains (Figures 4S and 4U), as well as the frequency of events per domain (19%) (Figure 4V), without affecting the amplitudes of Ca^{2+} transients (Figure 4W).

To determine whether $IP3R2$ -independent microdomain Ca^{2+} transients also occur in astrocytes in vivo, we monitored spontaneous and NE-induced Ca^{2+} transients in control ($GLAST-mGC3$) and $IP3R2^{-/-}$ mice ($GLAST-mGC3;IP3R2^{-/-}$) in primary visual cortex using two-photon imaging through a cranial window without anesthesia (Figure 5A). During quiet resting periods, V1 astrocytes exhibited periodic microdomain Ca^{2+} transients that were unsynchronized (Figures 5B–5E; Movie S4), similar to those observed in acute slices. Microdomain activity in astrocytes in $GLAST-mGC3;IP3R2^{-/-}$ mice in vivo was also attenuated relative to controls (Figures 5F and 5G; Movie S5), with fewer active domains (–64%) and fewer spontaneous events (–73%) observed during a comparable time period (Figure 5H; compare Figures 5D and 5E with Figures 5F and 5G). Astrocytes in primary visual cortex (V1) exhibit coordinated increases in cytosolic Ca^{2+} during locomotion, because NE is released when the state of arousal of the mice is increased (Paukert et al., 2014). In visual cortex, in vivo NE release led to a 4.5 \times increase in number of microdomain events (Figure 5I) and a 20% increase in mean amplitude of Ca^{2+} transients (Z score) (Figure 5J; Movie S4). In $IP3R2^{-/-}$ mice, enforced locomotion increased the frequency of microdomain events by 1.9 \times , but

did not alter their amplitude (Figures 5G, 5I, and 5J; Movie S5). These results indicate that periodic microdomain activity is an in vivo phenomenon that persists without $IP3R2$ -mediated Ca^{2+} release.

Microdomain Activity Does Not Require TRPA1

Recent studies have implicated TRPA1 as a primary mediator of microdomain activity and a contributor to resting Ca^{2+} levels in astrocytes (Shigetomi et al., 2011). However, exposure to the TRPA1 antagonist HC-030031 (50 μM) did not alter microdomain Ca^{2+} transients in astrocytes from $GLAST-mGC3;IP3R2^{-/-}$ mice (Figure S3G), although it induced a slight drop in the resting Ca^{2+} level (Figure S3H). Moreover, inhibiting other plasma membrane proteins implicated in contributing to astrocyte Ca^{2+} transients, including calcium release-activated channels (CRACs) (inhibited with GSK7975A), ryanodine receptors (inhibited with dantrolene), voltage-dependent Ca^{2+} channels (inhibited with CdCl_2), or Na^+ - Ca^{2+} exchangers (inhibited with benzamil and CGP37157), also did not block microdomain Ca^{2+} transients in astrocytes (Figure S3I). These results suggest that localized Ca^{2+} transients in astrocytes arise from an intracellular source capable of transiently storing and periodically releasing Ca^{2+} into the cytosol.

Microdomain Ca^{2+} Transients Co-localize with Mitochondria

When analyzing the localization of mGCaMP3 in astrocytes by immuno-EM, we noticed that mitochondria were often located adjacent to the plasma membrane (distance: 11.3 ± 4.1 nm), in close proximity to mGCaMP3 (Figures 6A and 6B), and occupied a substantial portion of the area within fine processes ($18\% \pm 4\%$) (Figures 6B and 6C), comparable with that occupied by mitochondria in excitatory nerve terminals ($16\% \pm 4\%$) (Figure 6C). To visualize the distribution of mitochondria in astrocytes, we generated a *Rosa26*-targeted knockin mouse line, in which the mitochondrial targeting of cytochrome c oxidase VIIIa (C8a) was fused to the N terminus of EGFP, allowing cell-specific labeling of mitochondria (Figures S4A and S4B) (see STAR Methods). These *Rosa26-lsl-mito-EGFP* (*mito-EGFP*) mice were crossed to $GLAST-CreER/+;Rosa26-lsl-tdTomato$ (Ai14) mice to also express cytosolic tdTomato (Figure S4C). Immunohistochemical analysis of these mice indicated that

(G–I) Graphs showing mean duration per event (G), frequency of events per domain (H), and spatial co-localization index (I) in control (+TTX) and NE (+TTX). Data are shown as mean \pm SEM ($n = 18$ cells, $GLAST-mGC3$ mice). *** $p < 0.0001$, paired two-tailed Student's t test.

(J) Map showing distribution of active microdomains recorded after application of ATP (blue) and NE (red). Microdomains that exhibited activity in both conditions are shown in green.

(K–M) Graphs comparing co-localization between microdomains recorded in NE (+TTX) and ATP (+TTX) (K), NE (+TTX) and DHPG (+TTX) (L), and ATP (+TTX) and DHPG (+TTX) (M). After randomization, the spatial co-localization of microdomains between two conditions was significantly reduced. Data are shown as mean \pm SEM. $n = 9$ cells from $GLAST-mGC3$ mice. *** $p < 0.0004$, paired two-tailed Student's t test.

(N) Graph of number of active domains per cell in control and during two successive applications of ATP (ATP1, ATP2). Data are shown as mean \pm SEM. $n = 15$ cells from $GLAST-mGC3$ mice. *** $p < 0.0001$; ** $p < 0.001$, repeated-measure one-way ANOVA analysis with Tukey's multiple comparisons post hoc test.

(O) Graph of spatial co-localization between active microdomains during two ATP applications. All experiments were done in the presence of TTX. After randomization, the spatial co-localization of microdomains between two conditions was significantly reduced. Data are shown as mean \pm SEM. $n = 15$ cells from $GLAST-mGC3$ mice. *** $p < 0.0001$, paired two-tailed Student's t test.

(P) Temporal correlation of Ca^{2+} transients among microdomains recorded during baseline (Control) and in the presence of metabotropic receptor agonists (ATP, DHPG, and NE; all in TTX). Data are shown as mean \pm SEM. $n = 9$ cells from $GLAST-mGC3$ mice. *** $p = 0.0002$, repeated-measures one-way ANOVA with Tukey's multiple comparison test.

See also Figure S2 and Movie S2.

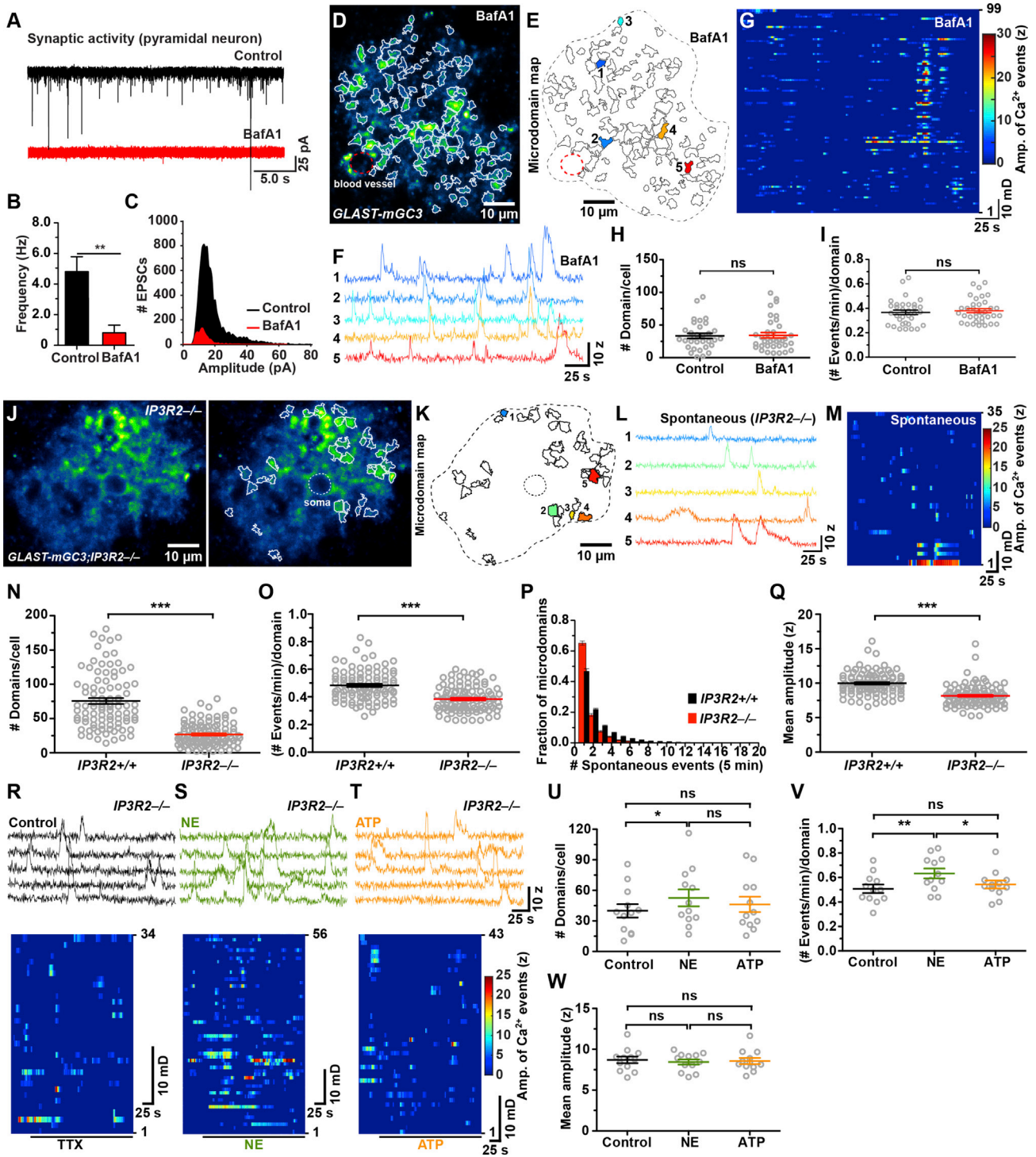


Figure 4. Spontaneous Microdomain Ca²⁺ Transients Persist in the Absence of Neurotransmitter Release and ER-Dependent Ca²⁺ Release

(A) Spontaneous EPSCs recorded from cortical pyramidal neurons in control conditions (black trace) and after treatment with veratridine (10 μM) and bafilomycin A1 (4 μM, BafA1, red trace).

(B) Histogram of the frequency of spontaneous EPSCs recorded in control conditions and after treatment with veratridine and BafA1. Data are shown as mean ± SEM. n = 7 (untreated) and n = 5 (BafA1) cells from control mice (*GLAST-mGc3* or *mGCaMP3/+*). **p < 0.009, unpaired two-tailed Student's t test.

(C) Histogram of the amplitudes of spontaneous EPSCs recorded in control conditions and after treatment with veratridine and BafA1.

(D) Image of one astrocyte from a *GLAST-mGc3* mouse showing median intensity projection (pseudocolored) from 540 frames (left) in an acute brain slice treated with veratridine and BafA1.

(legend continued on next page)

mitochondria were abundant in fine branches where microdomain Ca^{2+} transients occur (Figures 6D and 6E). Mitochondria have been shown to accumulate and release Ca^{2+} in a variety of cell types, including astrocytes (Rizzuto et al., 2012), raising the possibility that they contribute to cytosolic Ca^{2+} fluctuations within these compartments. To explore the spatial relationship between mitochondria and microdomain Ca^{2+} activity, we generated *GLAST-mG3;mito-EGFP* triple-transgenic mice and performed simultaneous time-lapse imaging of EGFP and mGCaMP3 (Figures 6F–6H; Movie S6). Because signals arising from mito-EGFP exhibit minimal intensity fluctuations (Figures S4D–S4G) and were largely stationary during the imaging period (Movie S6), they could be extracted from time-lapse movies, preserving the dynamic changes in mGCaMP3 in the vicinity of mitochondria (Figures 6F–6I; Figures S4H and S4I) (see STAR Methods). In control conditions (artificial cerebral spinal fluid [ACSF] + 1 μM TTX), 60% of spontaneous microdomain Ca^{2+} transients occurred at sites with mito-EGFP⁺ puncta, which increased to 85% when mitochondria 7 μm above and below the focal plane were included (Z-adjusted), accounting for the ability of Ca^{2+} to diffuse beyond mitochondria (Figure 6J). When the location of mito-EGFP⁺ puncta was randomized within the astrocyte volume, co-localization was reduced to 12% (Z-adjusted: 38%) (Figure 6J), suggesting that there is a specific association between mitochondria and regions where Ca^{2+} transients occur. Treatment with thapsigargin reduced the number of domains that were not co-localized with mitochondria (–mito domains) (Figure 6K), indicating that Ca^{2+} transients within these sites arise primarily from ER stores.

Transient Opening of the Mitochondrial Permeability Transition Pore Generates Microdomain Ca^{2+} Signals

Ca^{2+} homeostasis in mitochondria is achieved through mitochondrial $\text{Na}^+\text{-Ca}^{2+}$ (mNCX) and $\text{H}^+\text{-Ca}^{2+}$ (mHCX) exchangers, the mitochondrial Ca^{2+} uniporter (MCU), and the mitochondrial permeability transition pore (mPTP) (Bernardi and Petronilli, 1996). To determine if mitochondria contribute to spontaneous microdomain Ca^{2+} transients, we inhibited mitochondrial Ca^{2+} influx and efflux pathways using CGP37157 (20 μM) (to inhibit

mNCX and mHCX exchangers), cyclosporin A (20 μM) (to inhibit cyclophilin D, a component of the mPTP), and KB-R7943 (20 μM) (to inhibit MCU) (Rizzuto et al., 2012) in *GLAST-mG3;IP3R2^{-/-}* (Figures S5A–S5D), which EM analysis revealed had the same number and distribution of mitochondria in astrocyte processes as *IP3R2^{+/+}* mice (Figures S5E–S5G). Microdomain Ca^{2+} transients were virtually abolished in astrocytes from mice in the presence of these antagonists (Figures S5A and S5B), indicating that mitochondria participate in the generation of Ca^{2+} signals in astrocyte processes.

mPTP can act as a fast Ca^{2+} release channel (Bernardi and Petronilli, 1996), opening transiently to reset both Ca^{2+} and proton gradients across the mitochondrial inner membrane during periods of high respiration (Icha et al., 1997). mPTP is formed from multiple components, including ATP synthesis machinery and other transport and carrier proteins, but the molecular identity of the pore has not been determined. Although there are no antagonists of the pore, mPTP can be inhibited by blocking the activity of its constituent proteins, such as cyclophilin D. Treatment of cortical slices from *GLAST-mG3;IP3R2^{-/-}* mice with cyclosporin A (CsA; 20 μM) reduced the number of microdomains by 33%, the frequency of microdomain Ca^{2+} transients by 43%, and their amplitude by 17% (Figures S5H–S5J). However, cyclophilin D expression is much lower in astrocytes than neurons (Naga et al., 2007) (Figure S5K), which may explain partial inhibition by CsA. Thus, we applied CsA with rotenone (10 μM), a mitochondrial complex I blocker that has been used to inhibit mPTP activity in cells with reduced cyclophilin D (Li et al., 2012). Incubation of slices in these antagonists (mPTP-I solution) (Figure 7A) inhibited the frequency of microdomain Ca^{2+} transients by 70% (Figures 7B–7F; Movie S7), and the few events recorded in these antagonists were shorter in duration (control: 10.3 ± 0.9 s, $n = 18$; mPTP-I: 6.9 ± 0.5 s, $n = 18$; $p = 0.002$) and 20% smaller in amplitude (Figure 7F). Because the CaSCaDe analysis has a false-positive detection rate of about 5%–10% (Figures S1K–S1P), these results suggest that mPTP is critically involved in generating microdomain Ca^{2+} transients. To further test mitochondrial involvement, we disrupted the mitochondrial potential, because agents that collapse this

(E) Map of 99 spontaneously active microdomains recorded in veratridine and BafA1.

(F) Intensity versus time traces of five microdomains (corresponding to colors in E) showing characteristics of Ca^{2+} transients in veratridine and BafA1.

(G) Raster plot displaying Ca^{2+} transients from 99 microdomains in veratridine and BafA1.

(H and I) Graphs of number of microdomains per cell (H) and frequency of events per microdomain (I) recorded in control and in veratridine and BafA1. Data are shown as mean \pm SEM. $n = 33$ (untreated) and $n = 36$ (BafA1) cells from *GLAST-mG3* mice. ns, not significant; two-tailed Student's t test.

(J) Image of one astrocyte from a *GLAST-mG3;IP3R2^{-/-}* mouse showing median intensity projection (pseudocolored) from 260 s (left). Map of spontaneously active microdomains (in TTX, 1 μM) overlaid on image (right).

(K) Map of all spontaneously active microdomains in 260 s (35 domains). Dashed line indicates cell border.

(L) Intensity versus time traces of five microdomains (corresponding to colors in B) showing characteristics of Ca^{2+} transients.

(M) Raster plot displaying Ca^{2+} transients from active regions in 260 s.

(N–Q) Graphs of number of microdomains per cell (N), frequency of events per domain (O), number of Ca^{2+} transients observed per microdomain (P), and mean amplitude (Q) in *GLAST-mG3* (control, 94 cells) and *GLAST-mG3;IP3R2^{-/-}* (104 cells) mice. Data are shown as mean \pm SEM. *** $p < 0.0001$, unpaired two-tailed non-parametric Mann-Whitney test.

(R–T) Intensity versus time plots for five microdomains (top) and raster plots (bottom) displaying spontaneous Ca^{2+} transients in control (black) (R), NE (10 μM , green) (S), and ATP (100 μM , orange) (T) from *GLAST-mG3;IP3R2^{-/-}* mice. All experiments were done in the presence of 1 μM TTX.

(U–W) Graphs of number of microdomains per cell (U), frequency of events per domain (V), and mean amplitude (W) of spontaneous Ca^{2+} transients (in TTX, black) and NE (10 μM , green) and ATP (100 μM , orange) from *GLAST-mG3;IP3R2^{-/-}* mice.

Data are shown as mean \pm SEM. $n = 12$ cells for each condition. ns, not significant, $p > 0.05$; ** $p < 0.01$; * $p < 0.01$, repeated-measures one-way ANOVA analysis with Tukey's multiple comparisons post hoc test. See also Figure S3 and Movie S3.

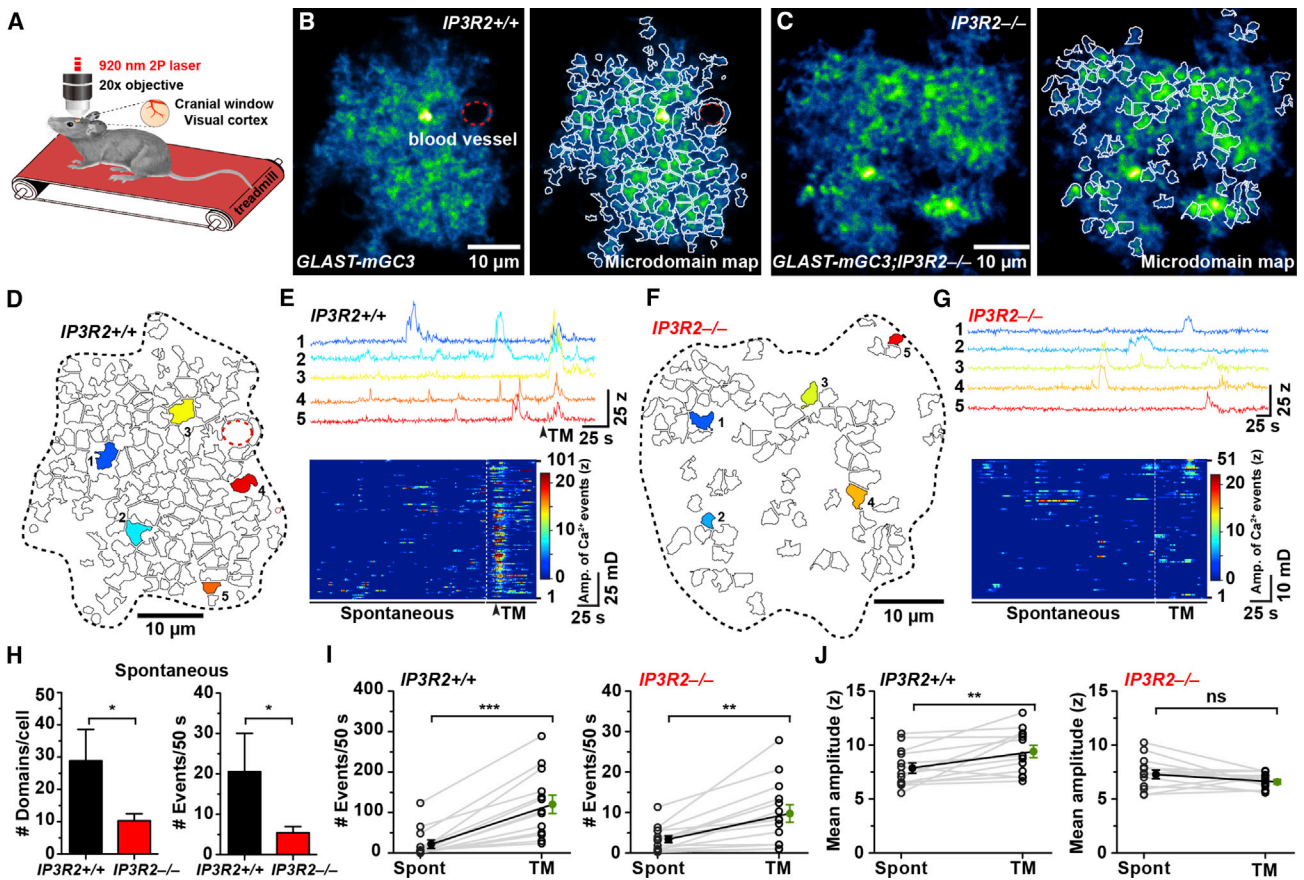


Figure 5. Microdomain Ca^{2+} Transients Persist In Vivo in $\text{IP3R2}^{-/-}$ Mice

(A) In vivo two-photon imaging configuration in which mice were allowed to walk on a linear treadmill.

(B) Median intensity projection image (pseudocolored) of one astrocyte in vivo from the primary visual cortex (V1) in a $\text{GLAST-mGC3};\text{IP3R2}^{+/+}$ mouse showing active regions during 260 s (left). Map of spontaneously active microdomains is overlaid on image (right). Dashed red line highlights blood vessel.

(C) Image of one astrocyte in vivo from visual cortex (V1) in a $\text{GLAST-mGC3};\text{IP3R2}^{-/-}$ mouse, showing median intensity projection (pseudocolored) from 260 s (left). Map of all spontaneously active microdomains (101) that occurred in 286 s is overlaid on image (right).

(D) Map of all microdomains (101) that occurred in 286 s in astrocyte shown in (B) ($\text{GLAST-mGC3};\text{IP3R2}^{+/+}$ mouse).

(E) Intensity versus time plots for five microdomains (corresponding to colors in D) showing characteristics of Ca^{2+} transients in a $\text{GLAST-mGC3};\text{IP3R2}^{+/+}$ mouse (top). Raster plot displaying the activity of all microdomains (bottom). Timing of enforced locomotion highlighted by dashed line.

(F) Map of all microdomains (51) that occurred in 286 s in astrocyte shown in (C) ($\text{GLAST-mGC3};\text{IP3R2}^{-/-}$ mouse).

(G) Intensity versus time plots for five microdomains (corresponding to colors in F) showing characteristics of Ca^{2+} transients from cell in (F) (top). Raster plot displaying the activity of all microdomains (bottom). Timing of enforced locomotion highlighted by dashed line.

(H) Histograms of the average number of active microdomains per cell (left) and number of Ca^{2+} transients (events) during 50 s of imaging (right) in $\text{IP3R2}^{+/+}$ ($\text{GLAST-mGC3};\text{IP3R2}^{+/+}$) and $\text{IP3R2}^{-/-}$ ($\text{GLAST-mGC3};\text{IP3R2}^{-/-}$) mice during baseline activity. Data are shown as mean \pm SEM. Fourteen cells from $\text{GLAST-mGC3};\text{IP3R2}^{+/+}$ mice and 25 cells from $\text{GLAST-mGC3};\text{IP3R2}^{-/-}$ mice were analyzed. ns, not significant; * $p > 0.05$, unpaired two-tailed Student's *t* test.

(I and J) Graphs showing the number of Ca^{2+} transients (events) observed during 50 s of imaging (I) and mean amplitude (Z score) for microdomain Ca^{2+} transients (J) without stimulation (spontaneous, Spont) and during enforced locomotion on the treadmill (TM) for control ($\text{IP3R2}^{+/+}$) (left) and $\text{IP3R2}^{-/-}$ mice (right). Data are shown as mean \pm SEM. Note change in scale for the $\text{IP3R2}^{-/-}$ mice in (I). Thirteen cells from $\text{GLAST-mGC3};\text{IP3R2}^{+/+}$ mice and 14 cells from $\text{GLAST-mGC3};\text{IP3R2}^{-/-}$ mice were analyzed. ns, not significant; $p > 0.05$, ** $p < 0.009$, *** $p < 0.0001$, paired two-tailed Student's *t* test.

See also [Movies S4](#) and [S5](#).

gradient block the transient opening of mPTP (Ichas et al., 1997) (Figure S5L). Acute application of the proton ionophore carbonyl cyanide 4-(trifluoromethoxy)phenylhydrazone (FCCP; 5 μM) (Figures S5M–S5P) reduced the number of microdomains by 56%, as well as the frequency by 68%, and amplitude of Ca^{2+} transients by 23% (Figures S5Q–S5S). Conversely, acute application of carboxyatractyloside (CAtr), which stimulates mPTP opening by inhibiting adenine nucleotide translocase (ANT) (Wang et al.,

2008) (Figure 7G), increased the number of active microdomains by 62% and the frequency of these events doubled, without affecting their amplitude (Figures 7H–7L).

To assess whether the effect of mPTP inhibitors on astrocytes was cell autonomous, we prepared pure cultures of cortical astrocytes from postnatal day (P) 7 (P7) $\text{GLAST-mGC3};\text{IP3R2}^{-/-}$ mice. Spatially restricted spontaneous Ca^{2+} transients (micro events) were observed that were distinct from larger events that

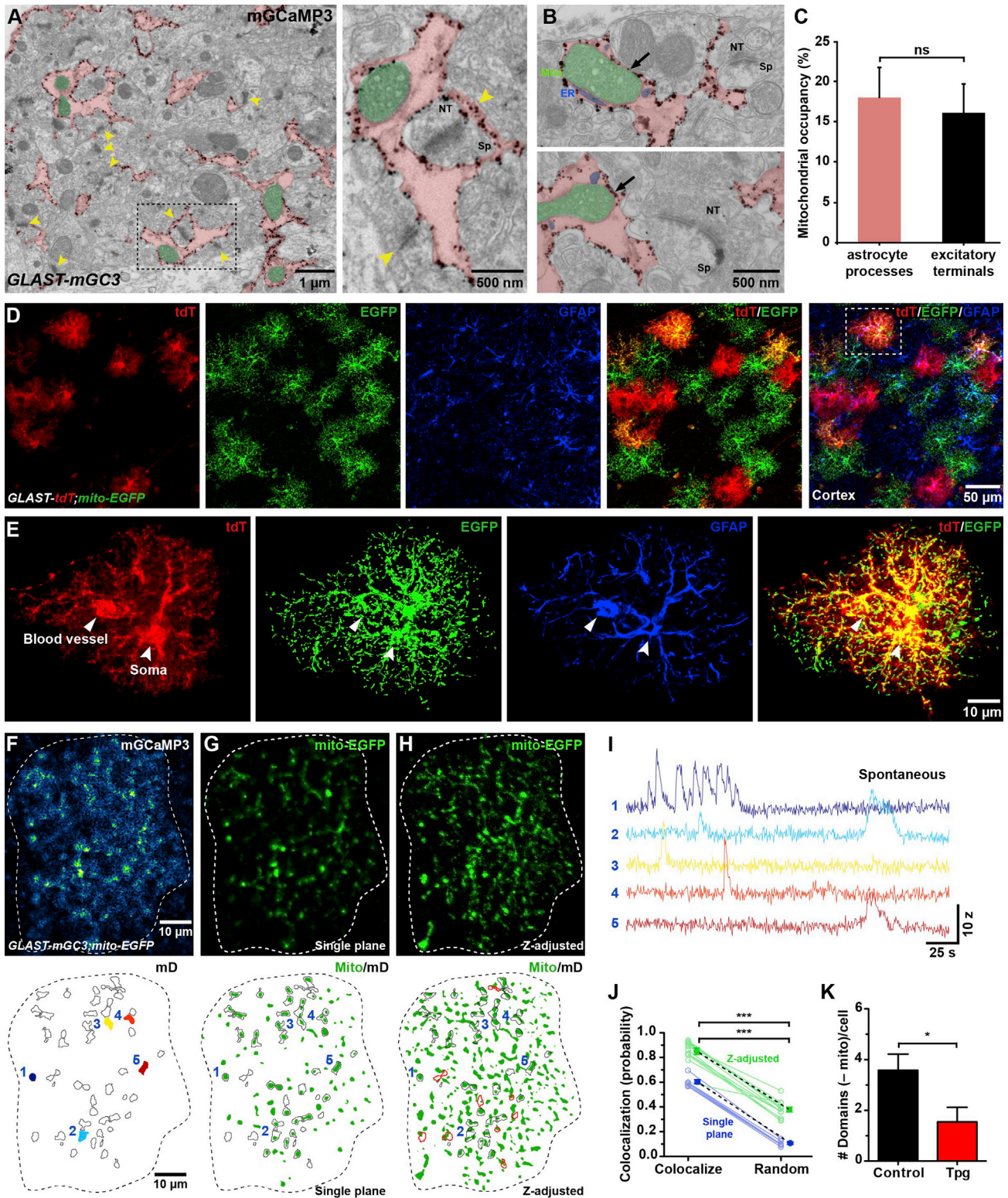


Figure 6. Microdomain Ca²⁺ Transients Co-localize with Mitochondria

(A) Electron micrograph showing silver-enhanced gold immunolabeling of mGCaMP3 in a *GLAST-mGC3* mouse. Astrocyte processes are colored red, and mitochondria in astrocyte processes are colored green. Yellow arrows highlight excitatory synapses. Image at right shows higher magnification image of area highlighted by boxed area at left.

(legend continued on next page)

propagated over long distances (macro events) (Figures S6A and S6B), with approximately half of the activity mediated by spatially restricted microdomains (size range: 5.5–22 μm^2) (Figure S6F). mPTP-I reduced the frequency of all Ca^{2+} transients by 56%, without altering their amplitude (Figures S6C and S6D), and the duration of events was prolonged by 38% (Figure S6E), consistent with a reduction in mitochondrial Ca^{2+} buffering. The frequency of micro events was reduced by 93% by mPTP-I (Figure S6G), and the duration of the remaining 7% of the events was prolonged by 46% (Figure S6G). However, larger Ca^{2+} transients (macro events) were preserved in the presence of mPTP-I (Figure S6F), indicating that these events are independent of IP3R2 and transient opening of mPTP. Notably, such large events were not observed in astrocytes in brain slices. Astrocytes retained the ability to exhibit a Ca^{2+} rise in response to ATP after treatment with mPTP-I (Figure S6H), and ATP-evoked events were prolonged in duration, providing additional evidence that mitochondria were unable to sequester Ca^{2+} after mPTP inhibition (Jackson and Robinson, 2015; Stephen et al., 2015).

To define the contribution of mPTP to spontaneous microdomain Ca^{2+} transients when IP3R2 is present, we measured inhibition by CsA and rotenone (mPTP-I) in cortical slices from control mice (*GLAST-mGC3*). mPTP inhibition reduced the number of active microdomains by 35%, as well as the frequency (–42%) and amplitude (–14%) of these Ca^{2+} events, whereas the duration of events remained unaltered (Figures S7A–S7D). Similar to the behavior of astrocytes in control animals, NE (+ mPTP-I) promoted a near-synchronous rise in Ca^{2+} in microdomains (compare Figures S7E and S7F with Figure 3E), increased the frequency of events by 59%, and enhanced the duration of events at each site by 33% (Figure 3G), but did not increase the amplitude of Ca^{2+} transients (Figure S3G), indicating that acute disruption of mPTP did not impair cell viability or their ability to engage in receptor-induced Ca^{2+} signaling (Figure S7E–S7G).

To overcome limitations associated with pharmacological manipulations, we developed a genetic approach to selectively

disrupt mitochondrial function in cortical astrocytes in vivo, by using the ability of the uncoupling protein 1 (UCP1), a component of mitochondria in brown fat cells, to create a proton (H^+) leak across the inner mitochondrial membrane and reduce the rate of oxidative phosphorylation (Krauss et al., 2005). We generated an adeno-associated virus (AAV8) packaged with $\Delta 9\text{UCP1}$, a variant of UCP1 that does not require fatty acid for H^+ transport (González-Barroso et al., 1997), and cytosolic mCherry under control of a human GFAP promoter (Figure S7H). Eight weeks after this virus was injected into the somatosensory cortex of *GLAST-mGC3* mice, astrocytes expressing $\Delta 9\text{UCP1}$ could be identified by expression of mCherry (Figure S7I), and both mutant (mCherry⁺) and control (mCherry[–]) astrocytes exhibited spontaneous microdomain Ca^{2+} transients (Figures S7J and S7K). Expression $\Delta 9\text{UCP1}$ reduced the frequency of events per domain by 24% and the amplitude of Ca^{2+} transients by 21% (Figures S7L and S7M), prolonged their duration (compare traces in Figures S7J and S7K and raster plots in Figure S7L), and increased the average domain size by 24% (Figure S7N), suggesting that mitochondrial Ca^{2+} buffering was impaired. This selective, genetic manipulation of astrocytes further supports the conclusion that mitochondria are an important contributor to microdomain Ca^{2+} transients in astrocyte processes.

Superoxide Production Enhances Microdomain Ca^{2+} Transients

Mitochondria exhibit periodic bursts of superoxide production during periods of high respiration that induce opening of mPTP (Wang et al., 2008), suggesting that ROS may be a key regulator of microdomain activity. To determine whether ROS production enhances microdomain Ca^{2+} transients by opening mPTP, we continuously illuminated astrocytes in slices from *GLAST-mGC3;IP3R2^{–/–}* mice for 5 min with 488 nm laser light (Figures 7M and 7N; Movie S8), a manipulation that induces ROS (Kuga et al., 2011). This manipulation doubled the number of active microdomains per cell and enhanced the number of events per microdomain by 39% (Figures 7M–7P), without changing their

(B) Electron micrographs showing spatial relationship between mitochondria and ER in astrocyte processes located in the vicinity of the excitatory nerve terminals.

(C) Histogram showing area within fine astrocyte processes and nerve terminals occupied by mitochondria. Data are shown as mean \pm SEM. ns, not significant; $p > 0.05$ unpaired two-tailed Student's t test.

(D) Images of cortical astrocytes from a *GLAST-CreER;Rosa26-*Isl-tdTomato*;Rosa26-*Isl-mito-EGFP** (*GLAST-tdT;mito-EGFP*) mouse labeled with anti-GFAP (GFAP, blue), anti-mCherry (tdT, red), and anti-GFP antibodies.

(E) High-magnification images of one astrocyte (highlighted by box in E) showing tdT, mGCaMP3, and GFAP localization.

(F) Image of one astrocyte in a *GLAST-mGC3;mito-EGFP* mouse showing median intensity projection (pseudocolored) from 260 s (top). Map of spontaneously active microdomains is overlaid on image (bottom). Dashed white line highlights cell border.

(G) Image of fluorescently tagged mitochondria from cell in (F) (top). Map of spontaneously active microdomains (mD, outlined in black) and mitochondria (Mito, green).

(H) Image of fluorescently tagged mitochondria in which z plane has been expanded to visualize mitochondria just above and below plane of imaging from cell in (F) (top). Map of spontaneously active microdomains (mD, outlined in black) and mitochondria (Mito, green). Additional co-localized areas are highlighted in red.

(I) Intensity versus time plots for Ca^{2+} transients from five microdomains (colors correspond to locations shown in F, bottom), showing characteristics of spontaneous Ca^{2+} signals.

(J) Plot of co-localization between spontaneously active microdomains and mitochondria, and co-localization after randomization of mitochondrial locations within the imaging plane (blue) and after z adjustment (green). Data are shown as mean \pm SEM. $n = 7$ cells (single plane) and $n = 12$ cells (z plane corrected) from *GLAST-mGC;mito-EGFP* mice. *** $p < 0.0001$, paired two-tailed Student's t test.

(K) Histogram showing the decrease in active microdomains that did not co-localize with mitochondria after treatment with thapsigargin (Tpg; 1 μM , 60 min) to deplete ER Ca^{2+} stores. Data are shown as mean \pm SEM, $n = 12$ (untreated) and $n = 11$ (Tpg-treated) cells. * $p < 0.03$, unpaired two-tailed Student's t test.

See also Figure S4 and Movie S6.

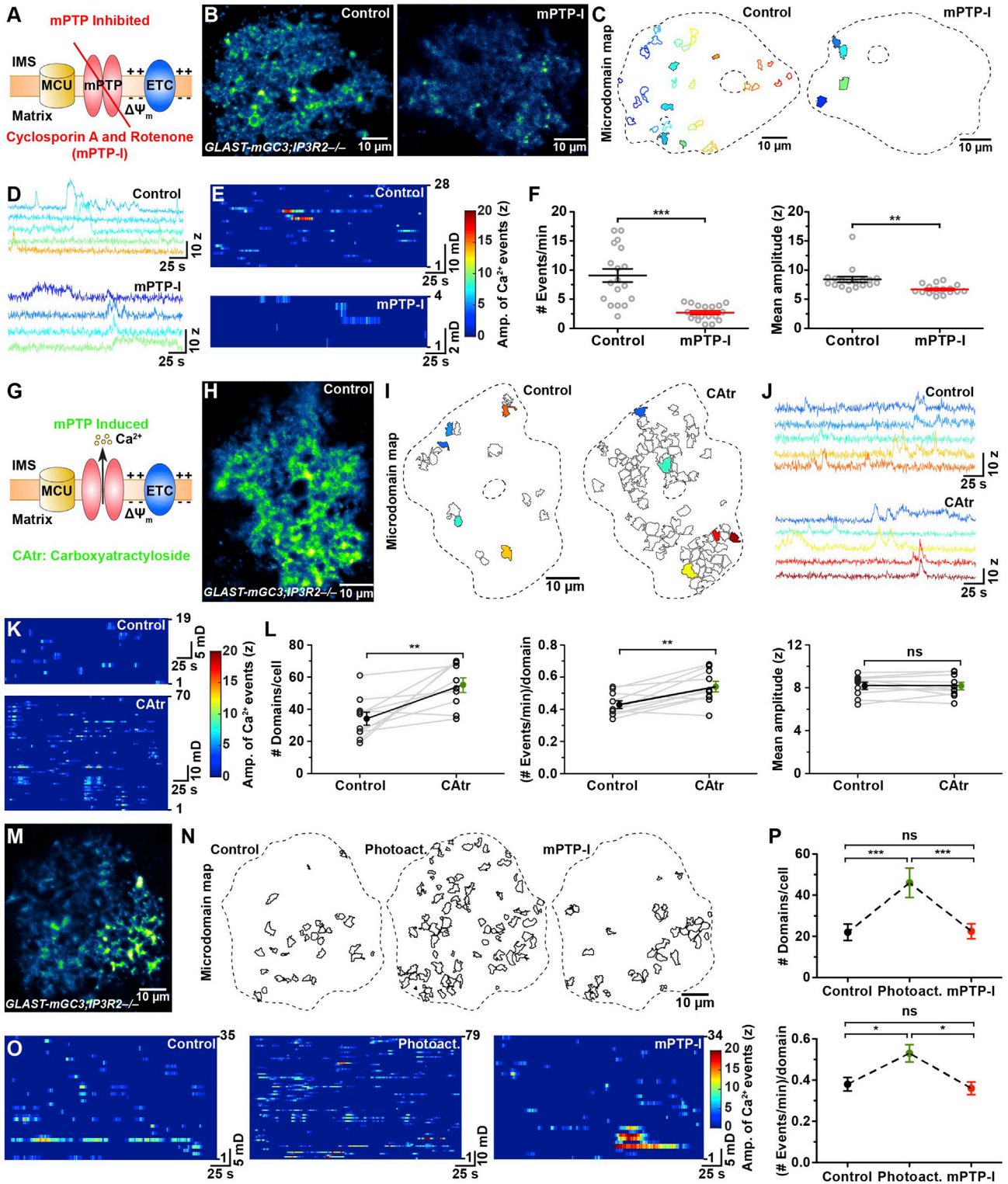


Figure 7. Mitochondrial Membrane Permeability Transition Pore Regulates Spontaneous Ca²⁺ Transients

(A) Schematic showing configuration of membrane permeability transition pore (mPTP, red), mitochondrial Ca²⁺ uniporter (MCU, yellow), and the electron transport chain (ETC, blue). Pharmacological inhibition of mPTP (mPTP-I; cyclosporin A, 20 μM, and rotenone, 10 μM) inhibits mPTP opening and prevents Ca²⁺ efflux from mitochondrial matrix into the cytosol.

(legend continued on next page)

amplitudes (control: $7.4 \pm 0.3z$, $n = 10$; +Photoactivation: $7.7 \pm 0.2z$, $n = 10$; $p = 0.29$). Subsequent exposure to mPTP-I markedly reduced this light-induced microdomain activity (Figures 7N–7P; Movie S8), indicating that ROS enhances mPTP-dependent Ca^{2+} efflux from mitochondria in astrocyte processes.

Mutations in the mitochondrial enzyme superoxide dismutase 1 (SOD1) in amyotrophic lateral sclerosis (ALS) induce mitochondrial stress and promote the dysfunction and eventual death of astrocytes and motor neurons (Liu et al., 2004). To determine whether mitochondrial dysfunction induced by overexpression of mutant SOD1 also alters mPTP gating and microdomain Ca^{2+} signaling in astrocytes, we performed in vivo Ca^{2+} imaging in the motor cortex of unanesthetized *GLAST-mGC3;SOD1^{G93A}* triple-transgenic mice when animals became symptomatic (~110 days of age) (Figure 8A). Astrocytes in the motor cortex of ALS mice exhibited higher microdomain activity (Figure 8B), with more active microdomains per cell (Figures 8C and 8D), and more events within each microdomain (Figure 8E) relative to age-matched controls. To determine whether mPTP hyperactivity contributes to this enhanced activity, we imaged mitochondria-induced microdomain Ca^{2+} transients in motor cortex slices of *GLAST-mGC3;SOD1^{G93A}* mice (aged ~120 days) in which ER Ca^{2+} stores were depleted with thapsigargin (Figures 8F–8I). Under these conditions, microdomain activity was enhanced by 87% in *SOD1^{G93A}* mice with a slight increase (14%) in the amplitude of events (Figures 8F–8J). Moreover, astrocyte activity in these animals exhibited greater inhibition (frequency: –42%; amplitude: –11%) by mPTP-I than controls (Figure 8K), suggesting that overexpression of mutant SOD1 enhances mPTP opening as a result of oxidative stress.

High Extracellular Glucose Enhances Microdomain Ca^{2+} Transients

Extracellular glucose levels may influence the degree to which mitochondria are mobilized to support ATP production, and

thereby alter mitochondrial Ca^{2+} efflux. Astrocytes in 1 mM glucose ACSF exhibited a comparable number of active microdomains, and the average amplitude of events at these sites was similar (Figures S8A–S8C); however, the frequency of Ca^{2+} transients in each microdomain was reduced by 18% (Figure S8B), as expected if the rate of oxidative phosphorylation (and opening probability of mPTP) was reduced. The frequency of neuromodulator-evoked microdomain Ca^{2+} transients was similarly enhanced by NE (10 μ M) in high- and low-glucose ACSF (Figure S8D), suggesting that fluctuations in extracellular glucose levels over this range do not alter the ability of this neuromodulator to stimulate mitochondrial activity.

Mitochondrial Ca^{2+} Efflux Is Enhanced by Neuronal Activity

The close link between mitochondrial respiration rate and Ca^{2+} efflux through mPTP suggests that increases in metabolic demand, such as that induced by neuronal activity may promote microdomain activity in astrocytes. To explore this possibility, we imaged astrocytes in cortical slices from *GLAST-mGC3;IP3R2^{-/-}* mice and enhanced neuronal activity by applying picrotoxin (100 μ M) (Figures S8E–S8I). Enhancing neuronal activity increased the number of microdomains by 52% and the frequency of Ca^{2+} transients by 62%, without affecting their amplitude (Figures S8J–S8L). This enhancement of microdomain activity was mediated by increased mPTP opening, as application of picrotoxin in the presence of mPTP inhibitors (Picro + mPTP-I) failed to enhance microdomain Ca^{2+} transients (Figures S8J–S8L). These results indicate that neuronal activity can promote cytosolic increases in Ca^{2+} in astrocytes independent of ER stores by promoting opening of mitochondrial mPTP, providing an explanation for ability of increases in arousal to enhance the frequency of microdomain activity in astrocytes in *IP3R2^{-/-}* mice (Figure 5) (Kanemaru et al., 2014; Srinivasan et al., 2015).

(B) Images of astrocytes (median intensity projection of time-series image stack) showing active regions during 286 s in control (left) and after exposure to mPTP-I (right) (*GLAST-mGC3;IP3R2^{-/-}* mouse).

(C) Maps of all spontaneously active microdomains in control (28) and after mPTP inhibition (4).

(D) Intensity versus time plots for five microdomains in control and four microdomains in mPTP-I treated slices (colors correspond to locations shown in C).

(E) Raster plot displaying Ca^{2+} transients from all active regions in 286 s in control (top) and mPTP-I (bottom)-treated slices.

(F) Graphs showing relative frequency (left) and mean amplitude (Z score) of Ca^{2+} transients in control and mPTP-I treated slices. Data are shown as mean \pm SEM. $n = 18$ cells. *** $p < 0.0001$; ** $p < 0.001$, unpaired two-tailed Student's t test.

(G) Schematic showing enhancement of mPTP opening by carboxyatractyloside (CAtr, 20 μ M), leading to enhanced Ca^{2+} efflux from the mitochondrial matrix to the cytosol.

(H) Image of an astrocyte (median intensity projection of time-series image stack) showing active regions during 286 s in a *GLAST-mGC3;IP3R2^{-/-}* mouse.

(I) Maps of all spontaneously active microdomains during 260 s in control (19) and after mPTP activation (70) (CAtr treated).

(J) Intensity versus time plots of microdomain activity in control (left) and after CAtr treatment (right) (colors correspond to locations shown in I).

(K) Raster plots displaying Ca^{2+} transients in an astrocyte in control (top) and after CAtr treatment (bottom).

(L) Graphs showing changes in number of active microdomains per cell (left), event frequency per microdomain (middle), and mean amplitude of Ca^{2+} transients (right) recorded in control and after CAtr treatment. Data are shown as mean \pm SEM. For each condition, 10 individual cells from *GLAST-mGC3;IP3R2^{-/-}* mice were analyzed. ** $p < 0.006$, paired two-tailed Student's t test.

(M) Image of an astrocyte (median intensity projection of time-series image stack) showing active regions during 286 s in a *GLAST-mGC3;IP3R2^{-/-}* mouse.

(N) Maps of all spontaneously active microdomains during 260 s in control (left), after light exposure (Photoact., middle), and after mPTP-I treatment (right).

(O) Raster plots displaying Ca^{2+} transients in an astrocyte in control (left), after light exposure (Photoact., middle), and after mPTP-I treatment (right).

(P) Graphs showing changes in number of domains per cell (top) and event frequency/domain (bottom) in control, after light exposure (Photoact.), and after mPTP-I treatment.

Data are shown as mean \pm SEM. $n = 10$ cells from *GLAST-mGC3;IP3R2^{-/-}* mice. *** $p < 0.0001$; * $p < 0.01$ repeated-measures one-way ANOVA analysis with Tukey's multiple comparisons post hoc test. ns, not significant. See also Figures S5, S6, and S7 and Movies S7 and S8.

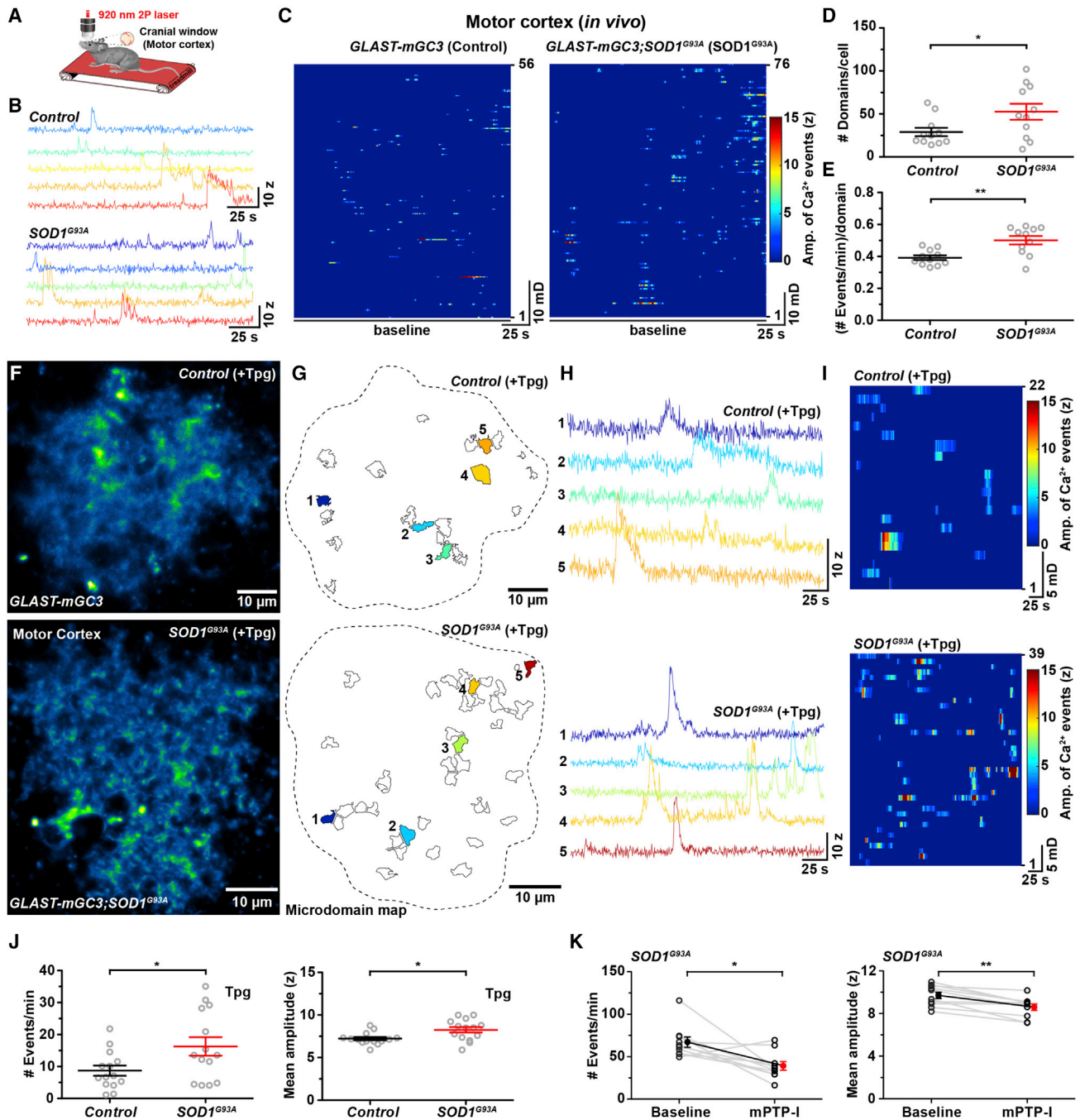


Figure 8. Enhanced Mitochondrial Ca^{2+} Efflux from Astrocytes in ALS Model (*SOD1^{G93A}*) Mice

(A) Schematic showing the in vivo two-photon imaging configuration in which mice were allowed to walk on a linear treadmill. (B) Intensity versus time plots of microdomain activity in an astrocyte from a control mouse (top) and from a *SOD1^{G93A}* mouse (bottom). (C) Raster plots displaying Ca^{2+} transients in astrocyte microdomains from a control mouse (left) and from a *SOD1^{G93A}* mouse (right). (D and E) Graphs of the number of active microdomains per cell (D) and frequency of events per microdomain (E) in control and *SOD1^{G93A}* mice. Data are shown as mean \pm SEM. $n = 11$ cells each from control and *SOD1^{G93A}* mice. * $p < 0.01$, ** $p < 0.001$, unpaired two-tailed Student's t test. (F) Images of single astrocytes in acute slices of motor cortex from a *GLAST-mG3* (top) and a *SOD1^{G93A}* mouse (bottom) showing median intensity projection (pseudocolored) from 260 s after treatment with thapsigargin (Tpg, 1 μM , 60 min). (G) Maps of all active microdomains (control: 22; *SOD1^{G93A}*: 39) that occurred in 286 s in astrocytes shown in (F). (H) Intensity versus time plots of microdomain activity in a control (top) and in a *SOD1^{G93A}* mouse (bottom) (colors correspond to locations shown in corresponding maps in G).

(legend continued on next page)

DISCUSSION

Mitochondria as a Source of Ca²⁺ in Astrocyte Microdomains

Astrocytes extend highly ramified processes that make contact with blood vessels, nodes of Ranvier, and synapses to facilitate ion redistribution, neurotransmitter uptake, and neuromodulation, activities that consume considerable energy (Bélanger et al., 2011). Regions where these events occur are often far removed from the cell body, because astrocyte processes consist of numerous thin lamellar extensions connected by narrow cytoplasmic bridges (Grosche et al., 1999). This complex geometry encourages functional isolation, but may also create local energetic demands. Although astrocytes are thought to use primarily glycolysis for ATP generation (Magistretti and Allaman, 2015), recent studies indicate that they contain numerous mitochondria and express enzymes necessary for oxidative phosphorylation (Hertz et al., 2007; Lovatt et al., 2007). By generating mice in which EGFP-tagged mitochondria were expressed only in astrocytes (Figures 6 and S4), we discovered that mitochondria are abundant in these thin processes, at a density comparable with that found in nerve terminals (Figure 6), where there is extraordinary metabolic demand.

In addition to producing ATP, mitochondria serve as a Ca²⁺ storage organelle that can profoundly influence intracellular signaling by buffering receptor-induced Ca²⁺ transients. During oxidative phosphorylation, the mitochondrial inner membrane periodically depolarizes because of reversible opening of mPTPs, non-selective pores that exhibit high Ca²⁺ permeability (Ichas et al., 1997). This periodic opening of mPTP dissipates pH gradients established during periods of high oxidative phosphorylation, enabling continued ATP production. mPTP opening is also associated with enhanced ROS production, events collectively referred to as “mitoflashes” (Wang et al., 2008). Mitoflashes have been observed in a variety of cell types, including neurons, cardiomyocytes, chondrocytes, and fibroblasts, and are highly conserved from worms to mammals (Hou et al., 2014), suggesting that they are a critical component of mitochondrial function. Simultaneous imaging of intracellular Ca²⁺ and fluorescently tagged mitochondria in astrocytes revealed that microdomain Ca²⁺ transients were spatially correlated with mitochondria (Figure 6). Moreover, inhibiting mPTP function in astrocytes (with CsA and rotenone) or disrupting the mitochondrial membrane potential (with FCCP), manipulations that decrease mitoflashes in other cells, markedly reduced microdomain Ca²⁺ transients (Figures 7 and S5), whereas enhancing mPTP opening (with CAtr) increased these transients (Figure 7). Notably, volatile anesthetics that inhibit mPTP also block astrocyte Ca²⁺ transients in vivo (Nimmerjahn et al., 2009). These effects of mPTP modulation appear to be mediated primarily within astrocytes, because they were also effective in purified astrocyte

cultures (Figure S6) and in brain slices from mice in which mitochondrial function was selectively disrupted in astrocytes by forcing expression of UCP1 (Figure S7).

The discovery that the low conductance “flickering” state of mPTP associated with mitoflashes also mediates Ca²⁺ efflux was enabled by the unique morphology of astrocytes. Because of membrane anchoring, mGCaMP3 was placed within 10 nm of mitochondria (Figure 6). Because of the close proximity of the Ca²⁺ sensor to mitochondria and the very small space in which Ca²⁺ can disperse, periodic Ca²⁺ efflux arising from brief openings of mPTP could be resolved. Such events would not be readily detected using cytosolic indicators, because of their low effective concentration in bulk solution and high endogenous Ca²⁺ buffering. Mitoflashes arising from individual mitochondria exhibit highly variable amplitudes and kinetics, and typically last for 10–20 s (Wang et al., 2008), comparable with the features of astrocyte microdomain Ca²⁺ transients (Figure 2), reflecting variations in the timing of mPTP opening and number of pores that are recruited within each mitochondrion. Together, these results suggest that the “cell-intrinsic” spontaneous Ca²⁺ transients that persist in astrocyte processes in the absence of IP3R-mediated Ca²⁺ release reflect stochastic opening of mPTP during periods of high oxidative phosphorylation. Notably, neuromodulators such as NE altered the duration of mPTP-elicited Ca²⁺ transients independent of ER-mediated Ca²⁺ release, suggesting that mPTP gating is modified during different behavioral states.

Functional Coupling between Mitochondria and ER Ca²⁺ Stores in Astrocytes

Spontaneous microdomain Ca²⁺ transients were markedly attenuated in *IP3R2*^{-/-} mice (Figures 4 and 5), an effect that was mimicked by depletion of Ca²⁺ stores with thapsigargin (Figure S3), suggesting that ER stores also contribute to this intrinsic activity. Mitochondria and ER are often in close proximity (<200 nm) and have been shown to form specialized junctions, “mitochondria-associated membranes” (MAMs), which facilitate direct exchange of ions and metabolites (Rizzuto et al., 1998). This close coupling may promote synergistic release of Ca²⁺. Indeed, interstitial cells of Cajal (ICC) in the gastrointestinal tract and submucosal cells in the colon exhibit rhythmic, spontaneous Ca²⁺ oscillations generated by Ca²⁺ exchange between ER Ca²⁺ stores and mitochondria (Ward et al., 2000; Yoneda et al., 2002) that are blocked when the electrochemical gradient across the inner mitochondrial membrane or IP3-dependent release of Ca²⁺ from ER stores are inhibited (Ward et al., 2000). Recent results suggest that activity in some astrocyte microdomains is dependent on extracellular Ca²⁺ influx (Rungta et al., 2016; Srinivasan et al., 2015), suggesting that mitochondrial Ca²⁺ is subject to homeostatic control or that there are also plasma membrane channels and/or transporters in these domains that enable Ca²⁺ influx independent of mitochondria.

(I) Raster plots displaying microdomain Ca²⁺ transients imaged over a period of 260 s recorded in Tpg in a control (top) and in a *SOD1*^{G93A} mouse (bottom).
 (J) Graphs comparing the frequency (left) and mean amplitude (Z score, right) of microdomain Ca²⁺ transients in Tpg-treated cortical slices from age-matched control and *SOD1*^{G93A} mice. Data are shown as mean ± SEM. n = 14 cells each from control and *SOD1*^{G93A} mice. *p < 0.03, unpaired two-tailed Student's t test.
 (K) Graphs comparing the frequency (left) and mean amplitude (Z score, right) of microdomain Ca²⁺ transients in *SOD1*^{G93A} mice before (baseline) and after mPTP inhibition (mPTP-I, 30 min). Data are shown as mean ± SEM. n = 10 cells each from control and *SOD1*^{G93A} mice. *p < 0.02, **p < 0.002, paired two-tailed Student's t test. See also Figure S8.

Our results suggest that ROS promote Ca^{2+} release in astrocyte microdomains, because this activity was dramatically enhanced by ROS, and chelating ROS or inhibiting mitoflash-associated ROS production attenuated microdomain Ca^{2+} transients (Figure 7). Mitochondria are the primary site of ROS production in cells, because of the continual loss of electrons from the electron transport chain during oxidative phosphorylation. Because ROS production is proportional to the rate of oxidative phosphorylation (Mailloux and Harper, 2012), the frequency of microdomain Ca^{2+} transients, like mitoflashes, provides an indication of the rate of ATP production in astrocyte processes. IP3R2 contains more than 50 cysteine residues for potential thiol-mediated oxidation, and recent studies show that physiologically relevant levels of $\text{O}_2\cdot^-$ stimulate opening of IP3R2 (Bánsághi et al., 2014), raising the possibility that mitochondria-derived ROS may act directly on IP3R2. In addition, we observed that expression of a mutant form of SOD1 (G93A) that causes mitochondrial stress enhanced mPTP opening and Ca^{2+} transients in astrocyte processes. Astrocytes exhibit reactive changes in $\text{SOD1}^{\text{G93A}}$ mice and have been shown to release factors that induce death of motor neurons (Nagai et al., 2007). This increase in Ca^{2+} signaling within astrocytes may contribute to secretion of neurotoxic molecules and accelerate neurodegeneration in ALS. Indeed, genetic deletion of cyclophilin D in $\text{SOD1}^{\text{G93A}}$ mice resulted in reduced astrocyte activation and enhanced motor neuron survival (Parone et al., 2013).

Functions of Localized Ca^{2+} Signaling in Astrocytes

Astrocytes have long been considered to be crucial for metabolic support of the CNS, by virtue of their association with blood vessels, their accumulation of glycogen, and their expression of monocarboxylic acid transporters that can export lactate, pyruvate, and ketone bodies to neurons for local production of ATP. Increasing neuronal activity reduces glycogen levels in astrocytes (Magistretti and Allaman, 2015), and inhibition of mitochondrial respiration with the gliotoxin fluoroacetate leads to swelling and fragmentation of ER, vacuolization, disruption of perivascular endfeet in astrocytes, and eventual neuronal degeneration (Paulsen et al., 1987), supporting the hypothesis that astrocytes play a key role in brain metabolism. However, the mechanisms that regulate ATP production within the highly ramified processes of astrocytes are not well understood. The ability to generate localized Ca^{2+} transients in these domains may facilitate ATP production by enhancing glycogenolysis (Verkerken et al., 1982), because elevation of Ca^{2+} activates glycogen phosphorylase, which is responsible for extracting glucose from glycogen. In hepatocytes, binding of epinephrine to α - and β -adrenergic receptors stimulates glycogenolysis by triggering release of ER Ca^{2+} and generating cAMP (Hems and Whitton, 1980), and a similar NE-mediated control of glycogenolysis occurs in cultured astrocytes (Magistretti and Allaman, 2015).

In the absence of an external stimulus, Ca^{2+} transients in different microdomains were uncorrelated, suggesting that mitochondrial activity is regulated locally within astrocyte processes. Moreover, the frequency of Ca^{2+} transients varied by an order of magnitude at different sites (Figure 2H), suggesting that local

rates of mitochondrial respiration, and thus metabolic demand, vary dramatically in different processes and can be modulated over a wide dynamic range. If mitoflash activity is a direct indication of mitochondrial respiration (Hou et al., 2014), then states of increased metabolic demand and cellular stress should enhance microdomain activity. Indeed, previous studies have shown that reactive astrocytes near amyloid plaques in mouse models of Alzheimer's disease have higher rates of spontaneous Ca^{2+} transients (Kuchibhotla et al., 2009), and our findings show that microdomain activity is similarly enhanced in astrocytes in $\text{SOD1}^{\text{G93A}}$ mice (Figure 8). Furthermore, conditions that increase neuronal firing in vivo, such as increased arousal during locomotion (Figure 5) (Kanemaru et al., 2014; Srinivasan et al., 2015), and in vitro, such as enhanced synaptic excitation during GABA receptor blockade (Figure S8), increased microdomain activity in the absence of IP3R2 signaling, providing evidence of a direct link between metabolic rate and microdomain Ca^{2+} transients.

Future studies involving selective manipulation of mitochondria within astrocytes will help define the roles of this ubiquitous form of Ca^{2+} signaling in the CNS in both health and disease.

STAR★METHODS

Detailed methods are provided in the online version of this paper and include the following:

- KEY RESOURCES TABLE
- CONTACT FOR REAGENT AND RESOURCE SHARING
- EXPERIMENTAL MODEL AND SUBJECT DETAILS
- TRANSGENIC ANIMAL MODELS
- METHOD DETAILS
 - Experimental Design
 - Targeting Vector for mGCaMP3 Conditional Allele
 - Targeting Vector for mitoEGFP Conditional Allele
 - Generation of mGCaMP3 and mitoEGFP Knockin Mouse Lines
 - Genotyping of mGCaMP3 and mitoEGFP Knockin Mouse Lines
 - Tamoxifen Injections
 - Immunohistochemistry
 - Immunoelectron Microscopy
 - Cortical Astrocyte Culture
 - Cloning and Generation of UCP1 Viral Vector
 - Viral Injections
 - Acute Brain Slice Preparation
 - Pharmacological Manipulations (See Key Resources Table)
 - Synaptic Current Recording and Analysis
 - Time-Lapse Fluorescence Imaging in Acute Brain Slices
 - In Vivo Two-Photon Microscopy
- QUANTIFICATION AND STATISTICAL ANALYSES
 - Automated Extraction and Analysis of Ca^{2+} Transients
 - Machine Learning-Based Signal Classification
- DATA AND SOFTWARE AVAILABILITY
 - Statistical Analysis

SUPPLEMENTAL INFORMATION

Supplemental Information includes eight figures, eight movies, and one data file and can be found with this article online at <http://dx.doi.org/10.1016/j.neuron.2016.12.034>.

AUTHOR CONTRIBUTIONS

A.A. and D.E.B. conceived the project, designed the experiments, and wrote the manuscript with help from the other authors. A.A. generated and characterized the *Rosa26-Is1-mGCaMP3* mice, conducted Ca^{2+} imaging and electrophysiology experiments, contributed to the development of CaSCaDe software, and analyzed data. P.-H.W. and D.W. designed and developed the CaSCaDe software. E.G.H. conducted *in vivo* Ca^{2+} imaging experiments. M.F. conducted immuno-electron microscopy and analyzed these data. M.A.T. generated the *Rosa26-Is1-mito-EGFP* mice. A.J.L. assisted with the experiments on cultured astrocytes and *in vivo* delivery of UCP1.

ACKNOWLEDGMENTS

We thank Dr. Jeremy Nathans (Johns Hopkins University) for assistance in generating mGCaMP3 and mito-EGFP mouse lines and for providing *GLAST-CreER* BAC transgenic mice. We thank Drs. Loren Looger and Tianyi Mao (Janelia Research Campus, HHMI) for the GCaMP3 construct, Dr. Ju Chen for providing IP3R2 null mutant mice (UCSD), Naiqing Ye for assistance with animal colony maintenance, and Holly Wellington and Chip Hawkins at the Johns Hopkins Transgenic Core for the assistance with generation of *Rosa26*-targeted mice. A.A. was supported in part by a Postdoctoral Fellowship (FG 1927-A-1) from the National Multiple Sclerosis Society and a NARSAD Young Investigator Grant (#24161) from the Brain & Behavior Research Foundation. This work was supported by grants MH084020 (Conte Center for Neuroscience) and NS050274 from the NIH and a grant from the Brain Science Institute at Johns Hopkins (to D.E.B.).

Received: November 12, 2015

Revised: October 4, 2016

Accepted: December 20, 2016

Published: January 26, 2017

REFERENCES

- Araque, A., Carmignoto, G., Haydon, P.G., Oliet, S.H.R., Robitaille, R., and Volterra, A. (2014). Gliotransmitters travel in time and space. *Neuron* *81*, 728–739.
- Bánsághi, S., Golenár, T., Madesh, M., Csordás, G., RamachandraRao, S., Sharma, K., Yule, D.I., Joseph, S.K., and Hajnóczky, G. (2014). Isoform- and species-specific control of inositol 1,4,5-trisphosphate (IP3) receptors by reactive oxygen species. *J. Biol. Chem.* *289*, 8170–8181.
- Bélangier, M., Allaman, I., and Magistretti, P.J. (2011). Brain energy metabolism: focus on astrocyte-neuron metabolic cooperation. *Cell Metab.* *14*, 724–738.
- Bernardi, P., and Petronilli, V. (1996). The permeability transition pore as a mitochondrial calcium release channel: a critical appraisal. *J. Bioenerg. Biomembr.* *28*, 131–138.
- Cavelier, P., and Attwell, D. (2007). Neurotransmitter depletion by bafilomycin is promoted by vesicle turnover. *Neurosci. Lett.* *412*, 95–100.
- Di Castro, M.A., Chuquet, J., Liaudet, N., Bhaukaurally, K., Santello, M., Bouvier, D., Tiret, P., and Volterra, A. (2011). Local Ca^{2+} detection and modulation of synaptic release by astrocytes. *Nat. Neurosci.* *14*, 1276–1284.
- Freeman, M.R., and Rowitch, D.H. (2013). Evolving concepts of gliogenesis: a look way back and ahead to the next 25 years. *Neuron* *80*, 613–623.
- Ganat, Y.M., Silbereis, J., Cave, C., Ngu, H., Anderson, G.M., Ohkubo, Y., Ment, L.R., and Vaccarino, F.M. (2006). Early postnatal astroglial cells produce multilineage precursors and neural stem cells *in vivo*. *J. Neurosci.* *26*, 8609–8621.
- González-Barroso, M.M., Fleury, C., Levi-Meyrueis, C., Zaragoza, P., Bouillaud, F., and Rial, E. (1997). Deletion of amino acids 261–269 in the brown fat uncoupling protein converts the carrier into a pore. *Biochemistry* *36*, 10930–10935.
- Grosche, J., Matyash, V., Möller, T., Verkhratsky, A., Reichenbach, A., and Kettenmann, H. (1999). Microdomains for neuron-glia interaction: parallel fiber signaling to Bergmann glial cells. *Nat. Neurosci.* *2*, 139–143.
- Gurney, M.E., Pu, H., Chiu, A.Y., Dal Canto, M.C., Polchow, C.Y., Alexander, D.D., Caliendo, J., Hentati, A., Kwon, Y.W., Deng, H.X., et al. (1994). Motor neuron degeneration in mice that express a human Cu,Zn superoxide dismutase mutation. *Science* *264*, 1772–1775.
- Haydon, P.G. (2001). GLIA: listening and talking to the synapse. *Nat. Rev. Neurosci.* *2*, 185–193.
- Hems, D.A., and Whitton, P.D. (1980). Control of hepatic glycogenolysis. *Physiol. Rev.* *60*, 1–50.
- Hertz, L., Peng, L., and Dienel, G.A. (2007). Energy metabolism in astrocytes: high rate of oxidative metabolism and spatiotemporal dependence on glycolysis/glycogenolysis. *J. Cereb. Blood Flow Metab.* *27*, 219–249.
- Hou, T., Wang, X., Ma, Q., and Cheng, H. (2014). Mitochondrial flashes: new insights into mitochondrial ROS signalling and beyond. *J. Physiol.* *592*, 3703–3713.
- Ichas, F., Jouaville, L.S., and Mazat, J.P. (1997). Mitochondria are excitable organelles capable of generating and conveying electrical and calcium signals. *Cell* *89*, 1145–1153.
- Jackson, J.G., and Robinson, M.B. (2015). Reciprocal regulation of mitochondrial dynamics and calcium signaling in astrocyte processes. *J. Neurosci.* *35*, 15199–15213.
- Kanamaru, K., Sekiya, H., Xu, M., Satoh, K., Kitajima, N., Yoshida, K., Okubo, Y., Sasaki, T., Moritoh, S., Hasuwa, H., et al. (2014). *In vivo* visualization of subtle, transient, and local activity of astrocytes using an ultrasensitive Ca^{2+} indicator. *Cell Rep.* *8*, 311–318.
- Khakh, B.S., and McCarthy, K.D. (2015). Astrocyte calcium signaling: from observations to functions and the challenges therein. *Cold Spring Harb. Perspect. Biol.* *7*, a020404.
- Kosaka, T., and Hama, K. (1986). Three-dimensional structure of astrocytes in the rat dentate gyrus. *J. Comp. Neurol.* *249*, 242–260.
- Krauss, S., Zhang, C.-Y., and Lowell, B.B. (2005). The mitochondrial uncoupling-protein homologues. *Nat. Rev. Mol. Cell Biol.* *6*, 248–261.
- Kuchibhotla, K.V., Lattarulo, C.R., Hyman, B.T., and Bacskai, B.J. (2009). Synchronous hyperactivity and intercellular calcium waves in astrocytes in Alzheimer mice. *Science* *323*, 1211–1215.
- Kuga, N., Sasaki, T., Takahara, Y., Matsuki, N., and Ikegaya, Y. (2011). Large-scale calcium waves traveling through astrocytic networks *in vivo*. *J. Neurosci.* *31*, 2607–2614.
- Li, X., Zima, A.V., Sheikh, F., Blatter, L.A., and Chen, J. (2005). Endothelin-1-induced arrhythmogenic Ca^{2+} signaling is abolished in atrial myocytes of inositol-1,4,5-trisphosphate(IP3)-receptor type 2-deficient mice. *Circ. Res.* *96*, 1274–1281.
- Li, B., Chauvin, C., De Paulis, D., De Oliveira, F., Gharib, A., Vial, G., Lablanche, S., Leverve, X., Bernardi, P., Ovize, M., et al. (2012). Inhibition of complex I regulates the mitochondrial permeability transition through a phosphate-sensitive inhibitory site masked by cyclophilin D. *Biochim. Biophys. Acta* *1817*, 1628–1634.
- Liu, J., Lillo, C., Jonsson, P.A., Vande Velde, C., Ward, C.M., Miller, T.M., Subramaniam, J.R., Rothstein, J.D., Marklund, S., Andersen, P.M., et al. (2004). Toxicity of familial ALS-linked SOD1 mutants from selective recruitment to spinal mitochondria. *Neuron* *43*, 5–17.
- Lovatt, D., Sonnewald, U., Waagepetersen, H.S., Schousboe, A., He, W., Lin, J.H.-C., Han, X., Takano, T., Wang, S., Sim, F.J., et al. (2007). The transcriptome and metabolic gene signature of protoplasmic astrocytes in the adult murine cortex. *J. Neurosci.* *27*, 12255–12266.
- Madisen, L., Zwingman, T.A., Sunkin, S.M., Oh, S.W., Zariwala, H.A., Gu, H., Ng, L.L., Palmiter, R.D., Hawrylycz, M.J., Jones, A.R., et al. (2010). A robust

- and high-throughput Cre reporting and characterization system for the whole mouse brain. *Nat. Neurosci.* **13**, 133–140.
- Magistretti, P.J., and Allaman, I. (2015). A cellular perspective on brain energy metabolism and functional imaging. *Neuron* **86**, 883–901.
- Mailloux, R.J., and Harper, M.-E. (2012). Mitochondrial proticity and ROS signaling: lessons from the uncoupling proteins. *Trends Endocrinol. Metab.* **23**, 451–458.
- Naga, K.K., Sullivan, P.G., and Geddes, J.W. (2007). High cyclophilin D content of synaptic mitochondria results in increased vulnerability to permeability transition. *J. Neurosci.* **27**, 7469–7475.
- Nagai, M., Re, D.B., Nagata, T., Chalazonitis, A., Jessell, T.M., Wichterle, H., and Przedborski, S. (2007). Astrocytes expressing ALS-linked mutated SOD1 release factors selectively toxic to motor neurons. *Nat. Neurosci.* **10**, 615–622.
- Nett, W.J., Oloff, S.H., and McCarthy, K.D. (2002). Hippocampal astrocytes in situ exhibit calcium oscillations that occur independent of neuronal activity. *J. Neurophysiol.* **87**, 528–537.
- Nimmerjahn, A., Mukamel, E.A., and Schnitzer, M.J. (2009). Motor behavior activates Bergmann glial networks. *Neuron* **62**, 400–412.
- Parone, P.A., Da Cruz, S., Han, J.S., McAlonis-Downes, M., Vetto, A.P., Lee, S.K., Tseng, E., and Cleveland, D.W. (2013). Enhancing mitochondrial calcium buffering capacity reduces aggregation of misfolded SOD1 and motor neuron cell death without extending survival in mouse models of inherited amyotrophic lateral sclerosis. *J. Neurosci.* **33**, 4657–4671.
- Paukert, M., Agarwal, A., Cha, J., Doze, V.A., Kang, J.U., and Bergles, D.E. (2014). Norepinephrine controls astroglial responsiveness to local circuit activity. *Neuron* **82**, 1263–1270.
- Paulsen, R.E., Contestabile, A., Villani, L., and Fonnum, F. (1987). An in vivo model for studying function of brain tissue temporarily devoid of glial cell metabolism: the use of fluorocitrate. *J. Neurochem.* **48**, 1377–1385.
- Petravicz, J., Fiacco, T.A., and McCarthy, K.D. (2008). Loss of IP3 receptor-dependent Ca²⁺ increases in hippocampal astrocytes does not affect baseline CA1 pyramidal neuron synaptic activity. *J. Neurosci.* **28**, 4967–4973.
- Rizzuto, R., Nakase, H., Darras, B., Francke, U., Fabrizi, G.M., Mengel, T., Walsh, F., Kadenbach, B., DiMauro, S., and Schon, E.A. (1989). A gene specifying subunit VIII of human cytochrome c oxidase is localized to chromosome 11 and is expressed in both muscle and non-muscle tissues. *J. Biol. Chem.* **264**, 10595–10600.
- Rizzuto, R., Pinton, P., Carrington, W., Fay, F.S., Fogarty, K.E., Lifshitz, L.M., Tuft, R.A., and Pozzan, T. (1998). Close contacts with the endoplasmic reticulum as determinants of mitochondrial Ca²⁺ responses. *Science* **280**, 1763–1766.
- Rizzuto, R., De Stefani, D., Raffaello, A., and Mammucari, C. (2012). Mitochondria as sensors and regulators of calcium signalling. *Nat. Rev. Mol. Cell Biol.* **13**, 566–578.
- Rungta, R.L., Bernier, L.P., Dissing-Olesen, L., Groten, C.J., LeDue, J.M., Ko, R., Drissler, S., and MacVicar, B.A. (2016). Ca²⁺ transients in astrocyte fine processes occur via Ca²⁺ influx in the adult mouse hippocampus. *Glia* **64**, 2093–2103.
- Schildge, S., Bohrer, C., Beck, K., and Schachtrup, C. (2013). Isolation and culture of mouse cortical astrocytes. *J. Vis. Exp.* **71**, e50079.
- Shigetomi, E., Tong, X., Kwan, K.Y., Corey, D.P., and Khakh, B.S. (2011). TRPA1 channels regulate astrocyte resting calcium and inhibitory synapse efficacy through GAT-3. *Nat. Neurosci.* **15**, 70–80.
- Shigetomi, E., Bushong, E.A., Hausteiner, M.D., Tong, X., Jackson-Weaver, O., Kracun, S., Xu, J., Sofroniew, M.V., Ellisman, M.H., and Khakh, B.S. (2013). Imaging calcium microdomains within entire astrocyte territories and endfeet with GCaMPs expressed using adeno-associated viruses. *J. Gen. Physiol.* **141**, 633–647.
- Srinivasan, R., Huang, B.S., Venugopal, S., Johnston, A.D., Chai, H., Zeng, H., Golshani, P., and Khakh, B.S. (2015). Ca²⁺ signaling in astrocytes from *Ip3r2(-/-)* mice in brain slices and during startle responses in vivo. *Nat. Neurosci.* **18**, 708–717.
- Stephen, T.L., Higgs, N.F., Sheehan, D.F., AlAwabdh, S., López-Doménech, G., Arancibia-Carcamo, I.L., and Kittler, J.T. (2015). Miro1 regulates activity-driven positioning of mitochondria within astrocytic processes apposed to synapses to regulate intracellular calcium signaling. *J. Neurosci.* **35**, 15996–16011.
- Tian, L., Hires, S.A., Mao, T., Huber, D., Chiappe, M.E., Chalasani, S.H., Petreanu, L., Akerboom, J., McKinney, S.A., Schreiner, E.R., et al. (2009). Imaging neural activity in worms, flies and mice with improved GCaMP calcium indicators. *Nat. Methods* **6**, 875–881.
- Ververken, D., Van Veldhoven, P., Proost, C., Carton, H., and De Wulf, H. (1982). On the role of calcium ions in the regulation of glycogenolysis in mouse brain cortical slices. *J. Neurochem.* **38**, 1286–1295.
- Wang, W., Fang, H., Groom, L., Cheng, A., Zhang, W., Liu, J., Wang, X., Li, K., Han, P., Zheng, M., et al. (2008). Superoxide flashes in single mitochondria. *Cell* **134**, 279–290.
- Ward, S.M., Ordog, T., Koh, S.D., Baker, S.A., Jun, J.Y., Amberg, G., Monaghan, K., and Sanders, K.M. (2000). Pacemaking in interstitial cells of Cajal depends upon calcium handling by endoplasmic reticulum and mitochondria. *J. Physiol.* **525**, 355–361.
- Yoneda, S., Takano, H., Takaki, M., and Suzuki, H. (2002). Properties of spontaneously active cells distributed in the submucosal layer of mouse proximal colon. *J. Physiol.* **542**, 887–897.

STAR★METHODS

KEY RESOURCES TABLE

REAGENT or RESOURCE	SOURCE	IDENTIFIER
Antibodies		
Goat polyclonal anti-mCherry	SICGEN	Cat# AB0040-200; RRID:AB_2333092
Goat polyclonal anti-GFP	SICGEN	Cat# AB0020-200; RRID:AB_2333099
Chicken polyclonal anti-GFP	Aves Labs	Cat# GFP-1020; RRID:AB_10000240
Rabbit polyclonal anti-GFAP	Dako	Cat# Z0334; RRID:AB_10013382
Rabbit polyclonal anti-GFP (for immuno-EM)	Frontier Institute	Cat# GFP-Rb-Af2020; RRID:AB_2571573
Donkey anti-Goat IgG (H+L), Alexa Fluor 488	Thermo Fisher Scientific	Cat# A-11055; RRID:AB_2534102
Donkey anti-Goat IgG (H+L), Alexa Fluor 546	Thermo Fisher Scientific	Cat# A11056; RRID:AB_10584485
Donkey anti-Rabbit IgG (H+L), DyLight 650	Thermo Fisher Scientific	Cat# SA5-10049; RRID:AB_2556629
Donkey anti-Chicken IgY (IgG) (H+L), Cy2	Jackson ImmunoResearch Labs	Cat# 703-225-155; RRID:AB_2340370
Goat anti-Rabbit Fab' fragment IgG, NANOGOLD (for immuno-EM)	Thermo Fisher Scientific	Cat# N24916; RRID:AB_10104359
Experimental Models: Mouse lines		
Tg(Slc1a3-cre/ERT)1Nat/J	Dr. Jeremy Nathans, Johns Hopkins	RRID:IMSR_JAX:012586
B6.Cg-Tg(GFAP-cre/ERT2)505Fmv/J	Jackson Laboratory	RRID:IMSR_JAX:012849
Itpr2tm1Chen/Itpr2+	Dr. Ju Chen, UC San Diego	RRID:MGI:3713675
B6SJL-Tg(SOD1*G93A)1Gur/J	Jackson Laboratory	RRID:IMSR_JAX:002726
B6;129-Gt(ROSA)26Sor(CAG-mGCaMP3)	This paper	N/A
B6;129-Gt(ROSA)26Sortm4(CAG-GFP*)Nat/J	This paper	RRID:IMSR_JAX:021429
B6;129S6-Gt(ROSA)26Sortm14(CAG-tdTomato)Hze/J	Jackson Laboratory	RRID:IMSR_JAX:007908
Chemicals (Pharmacological compounds)		
(S)-3,5-Dihydroxyphenylglycine, DHPG	Tocris	Cat# 0805; CAS:162870-29-3
Adenosine 5'-triphosphate magnesium salt	Sigma-Aldrich	Cat# A9187; CAS:74804-12-9
Bafilomycin A1	Enzo	Cat# BML-CM110-0100; CAS: 88899-55-2
Benzamil	Tocris	Cat# 3380; CAS:161804-20-2
Cadmium chloride	Sigma-Aldrich	Cat# 202908; CAS:10108-64-2
Carbonyl cyanide 4 (trifluoromethoxy)phenylhydrazone (FCCP)	Tocris	Cat# 0453; CAS:370-86-5
Carboxyatractyloside potassium salt	Calbiochem	Cat# 216201; CAS:35988-42-2
CGP 37157	Abcam	Cat# ab120012; CAS:75450-34-9
Cyclosporin A	Tocris	Cat# 1101; CAS:59865-13-3
Dantrolene, sodium salt	Tocris	Cat# 0507; CAS:14663-23-1
DL-TBOA	Tocris	Cat# 1223; CAS:205309-81-5
GSK-7975A	GlaxoSmithKline	N/A; CAS:1253186-56-9
HC 030031	Tocris	Cat# 2896; CAS:349085-38-7
KB-R7943 mesylate	Tocris	Cat# 1244; CAS:182004-65-5
L-(−)-Norepinephrine (+)-bitartrate salt monohydrate	Sigma-Aldrich	Cat# A9512; CAS:108341-18-0
Picrotoxin	Sigma-Aldrich	Cat# P1675; CAS:124-87-8
Rotenone	Tocris	Cat# 3616; CAS:83-79-4
Tetrodotoxin citrate	Abcam	Cat# ab120055; CAS:18660-81-6
Tamoxifen	Sigma-Aldrich	Cat# T5648; CAS:10540-29-1
Thapsigargin	Sigma-Aldrich	Cat# T9033; CAS:67526-95-8

(Continued on next page)

Continued

REAGENT or RESOURCE	SOURCE	IDENTIFIER
Veratridine	Tocris	Cat# 2918; CAS:71-62-5
Critical Commercial Assays		
Neural Tissue Dissociation Kit (P)	Miltenyi Biotec	Cat# 130-092-628
Recombinant DNA		
AAV8-hGFAP-mCherry-2A-Δ9UCP1-WPRE	This paper	N/A
Sequence-Based Reagents		
Primer: tcaatggcggggtcgtt (CMV-E-as)	(Paukert et al., 2014)	N/A
Primer: ctctgctgcctcctggctct (ROSA26 s)	(Paukert et al., 2014)	N/A
Primer: cgaggcggatcacaagcaata (ROSA26-as)	(Paukert et al., 2014)	N/A
Primer: cacgtgatgacaaccttgg (CaM-s)	This paper	N/A
Primer: ggcatataagcagcgtatcc (WPRE-as)	This paper	N/A
Software and Algorithms		
ZEN Blue/Black	Zeiss	RRID:SCR_013672
ImageJ	https://imagej.nih.gov/ij/	RRID:SCR_003070
Fiji	http://fiji.sc	RRID:SCR_002285
TurboReg	http://bigwww.epfl.ch/thevenaz/turboreg/	RRID:SCR_014308
MATLAB (R2014b)	MathWorks	RRID:SCR_001622
LIBSVM	http://www.csie.ntu.edu.tw/~cjlin/libsvm/	RRID:SCR_010243
pClamp 9.2	Molecular Devices	RRID:SCR_011323
MiniAnalysis	Synaptosoft Inc.	RRID:SCR_014441
Origin 8.0	OriginLab Corp.	RRID:SCR_014212
Prism 5.0	GraphPad Software	RRID:SCR_002798
Adobe Illustrator CS6	Adobe	RRID:SCR_014198
CaSCaDe	This paper	(see Data S1)

CONTACT FOR REAGENT AND RESOURCE SHARING

Dr. Dwight Bergles (dbergles@jhmi.edu) is the Lead Contact for reagent and resource sharing. All published reagents will be shared on an unrestricted basis; reagent requests should be directed to the lead author.

EXPERIMENTAL MODEL AND SUBJECT DETAILS

Both male and female mice were used for all experiments, and mice were randomly allocated to experimental groups. For ex vivo experiments, adult mice aged 7–12 weeks old were used and for in vivo experiments mice aged 15–20 weeks old were used, unless otherwise described. All mice (except end-stage *SOD1*^{G93A} mice) were healthy with no obvious behavioral phenotype, and none of the experimental mice were immune compromised. Except for *SOD1*^{G93A} animals, experimental mice were never involved in previous procedures or studies. For studies involving *SOD1*^{G93A} mice, mutant and littermate control mice were first imaged in vivo through a cranial window and then their brains were used for ex vivo slice physiology experiments. Since we used inducible Cre-loxP system (*GLAST-CreER*; *ROSA26-*Isl*-mGCaMP3*) to express mGCaMP3 in astrocytes, all experimental mice were injected with tamoxifen (for details, see Tamoxifen injections section below). Mice were maintained on a 12 hr light/dark cycle, and food and water was provided ad libitum. All animal experiments were carried out in a strict compliance with protocols approved by the Animal Care and Use Committee at the Johns Hopkins University School of Medicine.

TRANSGENIC ANIMAL MODELS

The conditional *Rosa26-*Isl*-mGCaMP3* and *Rosa26-*Isl*-mito-EGFP* mouse lines were generated by inserting a conditional allele into the ROSA26 locus (see Method details). Generation and genotyping of CreER driver lines *GLAST-CreER* (Paukert et al., 2014), *GFAP-CreER* (Ganat et al., 2006), tdTomato reporter mouse lines (Ai14, Allen Brain Institute) (Madisen et al., 2010), *IP3R2*^{-/-} null mutants (Li et al., 2005) and *SOD1*^{G93A} transgenic mice (Gurney et al., 1994) have been previously described.

METHOD DETAILS

Experimental Design

All ex vivo and in vivo experiments were replicated in more than nine cells derived from on an average 3 different mice (see figure legends for number of cells used for each experiments). In vitro experiments were repeated from at least two separate cohorts of mice, and more than ten coverslips were analyzed per condition. Most experiments were carried out in an unblinded manner and a specific randomization strategy was not used. However, in experiments where agonists were applied sequentially (such as ATP, DHPG and NE), the sequence of the drug application was randomized. Statistical computations were not performed to determine the optimal sample-size for experiments. Cells located on the surface of the brain slice, those that had large blood vessels passing through them, or exhibited image registration artifacts were excluded from the dataset.

Targeting Vector for mGCaMP3 Conditional Allele

To localize GCaMP3 to the plasma membrane we fused the gene sequence encoding the first 8 amino acids of the modified MARCKS sequence (MGCCFSKT) to the first methionine (i.e., start ATG) of GCaMP3 sequence (termed mGCaMP3). To enhance expression of mGCaMP3, we used a strong ubiquitous CMV- β -actin hybrid (CAG) promoter, which consists of three gene regulatory elements namely: 5' cytomegalovirus early enhancer element, chicken β -actin promoter and rabbit b-globin intron. For inducible expression of mGCaMP3, a loxP flanked 3X SV40 polyA with FRT flanked Neomycin gene (loxP-STOP-loxP, "Isl") "stopper" cassette was placed upstream of the coding sequence, preventing expression until cyclic recombinase (Cre) excises this gene sequence. To further enhance the expression of mGCaMP3, we sub-cloned the woodchuck hepatitis virus posttranscriptional regulatory element (WPRE) at the 3' end of mGCaMP3 expression sequence (Figure 1A). The WPRE sequence assists in quick exit of mRNA from the nucleus, and increases the mRNA stability in the cytosol.

Targeting Vector for mitoEGFP Conditional Allele

To localize EGFP to mitochondria, an N-terminal 25 amino acid targeting signal derived from mouse cytochrome c oxidase, subunit VIIIa (C8a) was fused to the N terminus of EGFP (termed mito-EGFP) (Rizzuto et al., 1989). To facilitate assessments of mito-EGFP localization, a V5 epitope tag was fused to EGFP at the C terminus. Similar to the strategy used for conditional expression of mGCaMP3, a stopper cassette containing a loxP flanked 3X SV40 polyA sequence was placed upstream of the mito-EGFP coding sequence, and the CAG promoter was used to control expression of mito-EGFP (Figure S4A).

Generation of mGCaMP3 and mitoEGFP Knockin Mouse Lines

To prevent gene-silencing effects and ensure consistent and long-term expression of these transgenes in all cell types, the CAG driven inducible mito-EGFP and mGCaMP3 transgenic constructs were targeted to the ubiquitously expressed ROSA26 locus. For homologous recombination in mouse embryonic stem (ES) cells, gene-targeting vectors for mito-EGFP and mGCaMP3 were assembled into a ROSA26 targeting plasmid containing a 2.3 kb 5' homology arm, 4.3 kb 3' homology arm, and PGK-DTA (Diphtheria toxin fragment A, downstream of 3' homology arm) for negative selection. ES cells, derived from a SV129 mouse strain, were electroporated with the *AsiSI* linearized targeting vectors. A nested PCR screening strategy along the 5' homology arm was used to identify ES cell clones harboring the correct genomic targeting event. To confirm proper targeting, Southern blot analysis was performed on EcoRI digested genomic DNA isolated from PCR positive ES cell clones and probed with a 494 bp long P³²-labeled probe located 123 bp upstream 5' homology arm of ROSA26 gene (Figure S4A). To confirm the integrity of the targeted ROSA26 locus, EcoRI digested ES cell genomic DNA was probed with P³²-labeled 475 bp probe located 2.9 kb downstream of 3' homology arm of ROSA26. After confirmation of the karyotypes, correctly targeted ES cell clones were used to generate chimeric mice by injection into blastocysts derived from SV129 females at the Johns Hopkins University Transgenic Core Laboratory. Germline transmission was achieved by breeding male chimeric founders to C57BL/6N wild-type female mice.

Genotyping of mGCaMP3 and mitoEGFP Knockin Mouse Lines

Routine genotyping of *Rosa26-Isl-mGCaMP3* mice was performed by PCR using following primers: ROSA26 s (5'-ctctgtcgcctcc tggctct-3'), ROSA26-as (5'-cgaggcggatcacaagcaata-3'), CaM-s (5'-cacgtgatgacaaaccttg-3') and WPRE-as (5'-ggcattaaagcagcgtatcc-3'). These primers amplify a 327bp DNA fragment for the wild-type ROSA26 allele, 245 and 327 bp fragments for heterozygous mGCaMP3 mice, and a single 245 bp fragment for homozygous mGCaMP3 mice. *Rosa26-Isl-mito-EGFP* mice were genotyped using following primers: ROSA26 s, ROSA26-as and CMV-E-as (5'-tcaatggcgggggtcgtt-3'). These primers amplify a 320bp DNA fragment for the wild-type ROSA26 allele, 250 and 320 bp fragments for heterozygous mito-EGFP mice, and a single 250 bp fragment for homozygous mito-EGFP mice. The *Rosa26-Isl-mito-EGFP* mouse line has been cryopreserved at the Jackson Laboratories (stock no: 021429).

Tamoxifen Injections

The tamoxifen solution for injections (@ conc. 10 mg/mL) was freshly prepared by sonicating tamoxifen freebase (T5648, Sigma-Aldrich) in sunflower seed oil (S5007, Sigma-Aldrich) at room temperature for 10-12 min (with intermittent 20 s vortexing every 3-4 min).

This solution was stored at 4°C for 5–7 days in a light protected condition or at –80°C for several months. Mice aged 3–4 weeks were intraperitoneally (i.p.) injected with tamoxifen at a dosage of 100 mg/kg body weight, once a day for two consecutive days, with each injection a minimum of 20 hr apart. All experiments were performed at least two weeks after the last tamoxifen injection.

Immunohistochemistry

6–8 weeks old mice were deeply anesthetized with pentobarbital and transcardially perfused with 4% paraformaldehyde (PFA) in 0.1 M sodium phosphate buffer (pH 7.4). Brains were isolated and post-fixed in 4% PFA for 16–18 hr at 4°C. After post-fixation, brains were stored in phosphate-buffered saline (PBS) containing 0.2% sodium azide at 4°C until further processed. 35 μ m thick free-floating coronal brain sections were cut using a vibratome (VT1000S, Leica), and sections were collected in PBS with 0.2% sodium azide and stored at 4°C. Before immunostaining sections were once rinsed in phosphate buffer saline (PBS), and then permeabilized for 10 min at room temperature (RT) in 0.3% Triton X-100 in PBS. Then to prevent binding of antibodies to non-specific epitopes, sections were incubated for 1 hr at RT in a blocking buffer (0.3% Triton X-100 and 5% normal donkey serum in PBS). For immunolabeling, sections were incubated with primary antibodies diluted in blocking buffer for 16–18 hr at 4°C on an orbital shaker. After rinsing at RT with PBS 3x for 5 min each, sections were incubated on an orbital shaker with fluorescent dye-conjugated secondary antibodies diluted in blocking buffer for 3 hr at RT. After rinsing 3x in PBS, sections were mounted on charged glass-slides and coverslipped in Aqua Ploy/Mount (Cat# 18606, Polysciences, Inc.). Primary antibodies used: goat anti-mCherry (1:5000, SICGEN), goat anti-GFP (1:5000, SICGEN), chicken anti-GFP (1:4000, Aves Lab, Inc.) and rabbit anti-GFAP (1:500, Dako). Secondary antibodies (raised in donkey): Alexa Fluor 488-, Alexa Fluor 546-, DyLight 650- or Cy2- conjugated secondary antibodies to rabbit, goat or chicken (1:500–1000, Thermo Fisher Scientific and Jackson ImmunoResearch). Images were acquired using a Zeiss LSM 510 Meta confocal microscope with a 25x (LD LCI Plan-Apochromat, Zeiss) or 63x (Plan-Apochromat, Zeiss) oil immersion objectives, and the pinhole set to 1 airy unit. Images represent maximum intensity projections of image stacks with a step size of 0.5 μ m. Low magnification images were acquired as a multi-tiled array using an epifluorescence microscope (Cell Observer, Zeiss) equipped with a computer controlled stage and a 10x air objective, and were aligned in Zen software (Zeiss). Images were then processed with ImageJ.

Immunoelectron Microscopy

For pre-embedding immuno-electron microscopy, *GLAST-mGC3* and *GLAST-mGC3;IP3R2^{-/-}* mice (16–17 weeks old) were transcardially perfused with 4% paraformaldehyde/0.1% glutaraldehyde in 0.1 M phosphate buffer (PB) under deep pentobarbital anesthesia. Brains, still within the skull, were post-fixed in the same fixative solution for 4 hr at 4°C. After post-fixation, brains were isolated and stored in 0.1 M PB with 0.05% sodium azide at 4°C until further processed. After blocking with 5% normal donkey serum in PBS, coronal sections (60 μ m in thickness) were incubated overnight with rabbit anti-EGFP IgG (Frontier Institute) and then with anti-rabbit IgG conjugated to 1.4 nm gold particles (Thermo Fisher Scientific). Following silver enhancement (HQ silver, Nanoprobes), sections were osmicated, dehydrated and embedded in Epon 812 resin. Ultrathin sections (70 nm in thickness) were prepared with an ultramicrotome (Leica Ultracut UCT) and stained with 2% uranyl acetate and 1% lead citrate. Electron micrographs were taken with an H-7600 electron microscope (Hitachi, Tokyo, Japan).

Cortical Astrocyte Culture

Primary cortical astrocytes were cultured according to standard protocols, modified from (Schildge et al., 2013). Briefly, cortices of P4–7 *GLAST-CreER;mGCaMP3^{+/+};IP3R2^{-/-}* triple transgenic mouse pups were dissociated using a Neural Tissue Dissociation Kit (P) (Miltenyi Biotec). Isolated cells were plated on a T-75 flask coated with poly-L-lysine (Sigma-Aldrich) and fed with DMEM (Life Technologies) supplemented with 10% heat-inactivated FBS (Life Technologies) and 1% penicillin-streptomycin (Life Technologies). After 7 days, astrocytes formed a confluent layer at the bottom of the flask. These cells were then plated on 12 mm cover glass (Thermo Fisher Scientific) coated with poly-L-lysine (Sigma-Aldrich) and Natural Mouse Laminin (Thermo Fisher Scientific) at a density of 20,000 cells per cover glass. One day after plating, expression of mGCaMP3 was induced by applying 1 μ M (Z)-4-hydroxytamoxifen (H7904, Sigma-Aldrich). At least 14 days later, astrocyte Ca²⁺ transients were imaged using a Zeiss LSM 710 microscope, as described below. To block mPTP activity, astrocyte cultures were incubated for 1 hr prior to Ca²⁺ imaging in mPTP inhibitors [Cyclosporin A (inhibits cyclophilin D, Tocris, 20 μ M; takes long time to dissolve and needs filtration of remaining precipitates) and Rotenone (Mitochondrial complex I inhibitor, Tocris, 10 μ M)].

Cloning and Generation of UCP1 Viral Vector

To specifically express the Δ 9 variant of the mouse uncoupling protein 1 (UCP1, genebank accession# NM_009463) (González-Barroso et al., 1997) in adult cortical astrocytes, this sequence was subcloned into a vector including a 2,178 bp human GFAP promoter fragment (exon1, genebank accession# M67446). To identify cells expressing Δ 9UCP1, a cytosolic variant of red-fluorescent protein mCherry was fused to the Δ 9UCP1 cDNA with the self-cleaving 2A peptide. To enhance the expression of mCherry and Δ 9UCP1, the woodchuck hepatitis virus posttranscriptional regulatory element (WPRE) was sub-cloned at the 3' end of the expression sequence (Figure S7H). The entire expression cassette (*hGFAP-mCherry-2A- Δ 9UCP1-WPRE*) was cloned into an adeno-associated virus serotype 8 (AAV8) viral vector.

Viral Injections

Adeno-associated virus was injected into adult mouse sensory cortex according to standard protocols. Briefly, 4 week old *GLAST-CreER;mGCaMP3/+* double transgenic mice were injected with tamoxifen to induce expression of mGCaMP3. Mice 18 weeks post injection were anesthetized using isoflurane (Baxter), immobilized in a stereotaxic instrument (Leica Biosystems) and a burr hole made above the somatosensory cortex using a micro-drill (Harvard Apparatus). Virus was targeted to the somatosensory cortex at 1.0 mm posterior and 3.0 mm lateral to Bregma. 1×10^9 viral genomes of *AAV8-hGFAP-mCherry-2A-Δ9UCP1-WPRE* were injected 600 μm below the pial surface using a Nanoject (Drummond Scientific) at 23 nL per second. Ten weeks after the injection, acute brain slices were prepared for Ca^{2+} imaging.

Acute Brain Slice Preparation

Mice were deeply anesthetized with isoflurane and decapitated using a guillotine. Their brains were dissected out and mounted on a vibratome (Leica VT100S) equipped with sapphire blade. Cortical slices 250 μm thick were cut in ice-cold N-methyl-D-glucamine (NMDG) based cutting solution, containing (in mM): 135 NMDG, 1 KCl, 1.2 KH_2PO_4 , 1.5 MgCl_2 , 0.5 CaCl_2 , 10 Dextrose, 20 Choline Bicarbonate, (pH 7.4). Cortical slices were then transferred to artificial cerebral spinal fluid (ACSF) containing (in mM): 119 NaCl, 2.5 KCl, 2.5 CaCl_2 , 1.3 MgCl_2 , 1 NaH_2PO_4 , 26.2 NaHCO_3 , and 11 Dextrose (292–298 mOsm/L) and were maintained at 37°C for 40 min, and at room temperature thereafter. Both NMDG solution and ACSF were bubbled continuously with 95% O_2 /5% CO_2 . All slice imaging experiments were carried out at room temperature.

Pharmacological Manipulations (See Key Resources Table)

For pharmacological manipulations involving thapsigargin (SERCA pump inhibitor, Sigma-Aldrich, 1 μM) and mitochondrial Ca^{2+} flux inhibitors [Cyclosporin A (inhibits cyclophilin D, Tocris, 20 μM; takes long time to dissolve in ACSF and requires filtration of remaining precipitates); Rotenone (mitochondrial complex I inhibitor, Tocris, 10 μM); KB-R7943 mesylate (inhibits mitochondrial Ca^{2+} uniporter, Tocris, 20 μM) and CGP37157 (inhibits mitochondrial $\text{Na}^+/\text{Ca}^{2+}$ exchanger, Abcam, 20 μM)], following recovery in ACSF at 37°C, brain sections were transferred to ACSF containing either drug or vehicle (DMSO) for 1 hr prior to Ca^{2+} imaging. To minimize the influence of neuronal activity on astrocyte Ca^{2+} signals, all pharmacological manipulations were performed in TTX (Na_v antagonist, Abcam, 1 μM), unless otherwise noted. To activate metabotropic receptors, adrenergic, glutamatergic or purinergic receptor agonists L-(–)-norepinephrine (Sigma-Aldrich, 10 μM); (S)-DHPG (group I metabotropic glutamate receptor agonist, Tocris, 20 μM) or ATP (purinergic receptor agonist, Sigma-Aldrich, 100 μM) were dissolved in ACSF and applied through the superfusing solution. The following agents were acutely applied by addition to the superfusing ACSF without pre-incubation: Carboxyatractyloside (mitochondrial ADP/ATP translocase inhibitor, Calbiochem, 20 μM); Picrotoxin (GABA_A receptor antagonist, Sigma-Aldrich, 100 μM); HC 030031 (TRPA1 channel antagonist, Tocris, 50 μM); Benzamil (plasma membrane $\text{Na}^+/\text{Ca}^{2+}$ exchanger inhibitor, Tocris, 100 μM); Dantrolene (ryanodine receptor antagonist, Tocris, 10 μM); Carbonyl cyanide 4-(trifluoromethoxy)phenylhydrazone (FCCP, uncoupler of oxidative phosphorylation, Tocris, 5 μM); GSK7975A (Orai/ I_{crac} blocker, gift from GlaxoSmithKline, 10 μM).

Synaptic Current Recording and Analysis

Cortical pyramidal neurons were visualized with an upright microscope (Zeiss Axioskop2 FS plus) equipped DIC optics and a CCD camera (Sony XC-73). Acute brain slices were prepared from either *mGCaMP3/+* or *GLAST-CreER/+;mGCaMP3/+* mice, as described above. Whole-cell recordings in voltage-clamp configuration were made under visual control using IR-DIC imaging, using pipettes filled with (in mM): 100 CsCH_3SO_3 [cesium methanesulfonate], 20 tetraethylammonium chloride, 20 HEPES, 1 MgCl_2 , 10 EGTA, 2 Na_2ATP , and 0.2 NaGTP (pH 7.3, 295 mOsm). Pipette resistance was 3.8 – 4.2 MΩ and recordings were made without series resistance compensation. Baseline synaptic activity was assessed by recording spontaneous EPSCs (sEPSCs) at a holding potential of –80 mV (corrected for the junction potential) for 5 min in gap-free mode. To block vesicular release of neurotransmitters, following recovery in ACSF at 37°C for 40 min, acute brain slices were transferred to ACSF containing veratridine (voltage gated Na_v opener, Tocris, 10 μM) for 5 min and then incubated in bafilomycin A1 (vesicular H^+ -ATPase inhibitor, Enzo, 4 μM) for at least 2.5 hr at room temperature (Cavelier and Attwell, 2007). While performing whole-cell voltage-clamp recordings of EPSCs (for 5 min), bafilomycin A1 (2 μM) and TTX (1 μM) were applied throughout the experiment by recirculating continuously oxygenated ACSF containing these drugs using a peristaltic pump (Watson-Marlow Alitea, Sci-Q, 400 series).

Responses were recorded using a MultiClamp 700A amplifier (Molecular Devices), filtered at 3 kHz, digitized at 10 kHz and recorded to disk using pClamp9.2 software (Molecular Devices). Data were analyzed offline using Clampfit (Molecular Devices), Origin (OriginLab) and Mini analysis (Synaptosoft) software. Input resistance and membrane capacitance were calculated from a 10 mV depolarizing step from a holding potential of –80 mV; experiments in which the input resistance changed by more than 15% were excluded. Data are expressed as mean SEM throughout, and statistical significance was determined using the paired two-tailed Student's test with a cutoff value of 0.05 and the Kolmogorov–Smirnov (KS) test for cumulative distributions.

Time-Lapse Fluorescence Imaging in Acute Brain Slices

Fluorescence changes arising from mGCaMP3, tdT or mito-EGFP were recorded from individual cortical astrocytes using a Zeiss LSM 710 microscope with 20x (NA 1.0) water immersion objective (Zeiss), using the 488 nm or 543 nm laser lines. Slices were continuously superfused with ACSF bubbled with 95% O_2 /5% CO_2 . Astrocytes are extremely photosensitive and exhibit increased Ca^{2+}

transients when exposed to laser light (Kuga et al., 2011). Therefore, astrocytes were imaged at a low laser power of 29 μ W, with no pixel averaging, high PMT gain (\sim 800), and with a pinhole size of 2.69 airy units, corresponding to 3.6 μ m of z-depth. For each experimental session, individual astrocytes (\sim 3500–4900 μ m²) were imaged at the pixel depth of 8 bit with a resolution of 512 \times 512 pixels. Individual imaging sessions consisted of 600 frames at a frame scan rate of 2.1 Hz (0.484 s/frame). For laser induced photo-activation, cells were imaged using a 488 nm laser at 116 μ W power for 5 min. To compensate for minor drift in the XY plane, image stacks were post hoc registered using TurboReg (plugin for ImageJ) for automatic alignment of images. During registration of 8-bit images TurboReg transforms images into a 32-bit format. After registration, images were reformatted to 16-bit, as reverting back to 8-bit blunted signal amplitudes. Surrounding background pixels that were not part of the cell (based on median-intensity projection of the image stack) were cropped to accelerate analysis. Astrocytes located on the surface of the slice, those that had large blood vessels passing through them, or exhibited image registration artifacts were excluded from the dataset.

In Vivo Two-Photon Microscopy

Mice aged 2–4 months were implanted with cranial windows, as described (Paukert et al., 2014). Mice were anesthetized with isoflurane (induction, 5%; maintenance, 1.5%–2.0%, mixed with 0.5 l/min O₂) and their body temperature was monitored and maintained at 37°C with a thermostat-controlled heating pad. An incision was made over the right cerebral hemisphere, the skin retracted, and the skull cleaned. A 2 \times 2 mm region of skull over the visual cortex (centered at lambda and 3.5 mm lateral from the midline) was removed using a scalpel. A 2 \times 2 mm piece of cover glass (VWR, No. 1) was placed within the craniotomy, sealed, and a 9 mm-wide aluminum head plate with a 5 mm circular opening was attached to the skull using dental cement (C&B Metabond; Parkell Bio-Materials Div.). In vivo imaging sessions began 3–4 hr after surgery, following complete recovery from anesthesia. During an imaging session, the head of the mouse was immobilized by attaching the head plate to a custom machined stage fitted with a freely-movable linear treadmill. Mice were kept on the stage for a maximum of two hours. Fluorescence images were collected using a Zeiss LSM 710 microscope equipped with a Zeiss 20x, 1.0 NA objective. Two photon excitation was achieved using a mode-locked Ti:sapphire laser (Coherent Ultra II) tuned to 920 nm. Each image frame was acquired at the rate of 0.484 s/frame (about 2.1 Hz) and was approximately 60 μ m \times 60 μ m at 512 \times 512 pixel resolution. The average power at the sample did not exceed 20 mW during the imaging session.

QUANTIFICATION AND STATISTICAL ANALYSES

Automated Extraction and Analysis of Ca²⁺ Transients

We developed an algorithm to identify and extract kinetic information about individual microdomain activity in MATLAB (Mathworks, Natick, MA). To remove background noise, 3D convolutions were performed using average and Gaussian filters of size 23 \times 23 \times 43 pixels (x,y,t) on time-series image stacks (I(x,y,t)). Then a noise filtered image stack (I_{fil}(x,y,t)) was obtained by subtracting the 3D convolution products of average and Gaussian filtering. To determine the locations of regions exhibiting dynamic changes in fluorescence, the mean intensity (I_{bg}) and standard deviation (σ_{bg}) of background pixels on sum-intensity projected noise filtered stacks (I_{fil}(x,y,t)) was calculated. Next, the sum-intensity projected image was binarized using a threshold value of I_{bg} + 2* σ_{bg} . After smoothing the image with a 43 \times 43 pixels² Gaussian filter and standard deviation of 3 pixel, regional maximas were detected on the sum-intensity projected image. To generate a mask of putative microdomains, all microdomains with more than two regional maxima using a marker-controlled watershed segmentation method were segmented, and microdomains with an area less than 5 \times 5 pixels² were considered at noise level and removed from the binarized image. Then based on this binarized mask of potential microdomains, the intensity level over time of individual microdomains from the raw time series image stack I(x,y,t) was plotted. The intensity profile of each microdomain was normalized by subtracting the mean intensity value of its background and then to rescale, this value was divided by the standard deviation of the background. In this study, this value is represented as a modified z-score (z). Microdomain events were then automatically detected based on the following criteria: to consider an event to be positive it must consist of a regional maximum of more than 5.0 a.u. within 4 neighboring frames, the beginning and end time point of each event was identified based on the time point prior to or after the peak that had an intensity value larger than 0.5 a.u. Events that spanned less than 4 frames were excluded.

Machine Learning-Based Signal Classification

The Support Vector Machine (SVM) algorithm was used to detect active microdomains based on 75 parameters of each individual event. These parameters were extracted from a raw and two smoothed intensity profiles with different degree of smoothness. The smoothed intensity profiles were obtained from the difference between convolving raw intensity profiles with a Gaussian filter with unit standard deviation and an averaging filter of the same size. Two smoothed intensity profiles were obtained using filters of size 11 and 21 frames separately. Twenty-five parameters each were used to describe each individual event with these three intensity profiles. For initial training, the SVM algorithm was provided a set of 2500 fluorescence signals manually categorized as positive or negative, and various parameters of these events were normalized to a range between 0 and 1. These normalized parameters were used to generate a SVM model using libsvm. This SVM prediction model was applied to all events, and events classified as negative by libsvm were excluded. The overall accuracy from SVM prediction was > 85%, assessed by comparing the predicted results from an additional set of manually registered 2500 events, and \sim 95% based on fluctuations in Ca²⁺-insensitive fluorescent protein tdTomato (Figures S1K–S1P).

DATA AND SOFTWARE AVAILABILITY

The MATLAB code for CaSCaDe analysis routine (outlined above) is provided as supplemental text (see [Data S1](#)).

Statistical Analysis

Statistical analyses were performed using GraphPad Prism (version 5.0b) and Origin 8 (OriginLab Corp). All datasets were tested for Gaussian distribution with the D'Agostino-Pearson "omnibus K2" normality test. If one of the two or both the datasets passed the normality test, a two-tailed unpaired t test was used to compare the significance difference in means between the two groups, otherwise a nonparametric test (Mann-Whitney test) was chosen. For multiple group datasets, one-way ANOVA analysis was used, followed by Tukey's multiple comparison tests for more than two groups. When two or more consecutive experiments were performed on the same cell, then a two-tailed paired t test or a repeated-measure ANOVA analysis followed by Bonferroni correction for multiple comparisons was carried out. Statistical tests used to measure significance are indicated in each figure legend along with the corresponding significance level (p value). For all ex vivo and in vivo experiments, N represents number of cells analyzed per experiment and the exact value of N is provided in the corresponding figure legends. For in vitro experiments ([Figure S6](#)), N represents number of 12 mm coverslips on which cells were grown and n represents number of cells analyzed per condition. In vitro experiments were repeated from at least two separate cohorts of mice. Data are reported as mean \pm SEM and $p < 0.05$ was considered statistically significant.